



LUND UNIVERSITY
Faculty of Science

Exploring the Use of Graphene as a Target Material for Laser Plasma Ion Acceleration

Hannes Pahl

Thesis submitted for the degree of Master of Science
Project duration: 5 months

Supervised by Claes-Göran Wahlström

Department of Physics
Division of Atomic Physics
January 2017

Lund Reports on Atomic Physics, LRAP 533 (2017)

Abstract

The interaction of a solid target with an ultra-high intensity laser pulse can result in the laser plasma acceleration of ions. The recent proposal of a new laser plasma ion acceleration scheme, named chirped standing wave acceleration, has created interest in a new class of ultra-thin solid target materials, either freestanding or as a part of novel compound targets. In this thesis, it is assessed, if it is feasible to use targets made of freestanding graphene, a carbon allotrope consisting of only one or a few atomic layers.

For this purpose, a target system was developed to mount freestanding graphene in the ion acceleration experiment at the Lund Laser Centre, and commercially available graphene targets were put to a number of tests. Using the Lund Terawatt Laser, the threshold for laser induced damage of the targets was determined. Further, freestanding graphene targets were exposed to ultra-high intensity laser pulses, in order to evaluate the effect on these ultra-thin samples and the supporting structure. The conditions were similar to those in conventional laser plasma acceleration experiments. For analysis and alignment purposes, the targets were imaged using an existing on-line microscope system, and the steps required to extend the imaging system with a Raman spectroscopy setup were explored.

The specially designed and constructed target mounting system was found to work reliably, and the graphene targets used in this project were found to be robust enough to be handled in the experimental environment. While the Raman spectroscopy was not fully implemented, the microscope system was extensively used and found capable to reveal occasional imperfections of the freestanding graphene samples. The damage threshold fluence was found to be approximately 0.1 J/cm^2 for the graphene targets. In the ultra-high intensity shots, small damage was inflicted to the frame supporting the graphene, and particle acceleration was observed. Accelerated ions were recorded with nuclear track detectors. They show traces of protons with energies above 1 MeV, and some signals also of heavier ions. The acceleration is attributed to a target normal sheath acceleration-like process, possibly involving the graphene-supporting copper grid, but the limited data does not allow a definite interpretation.

The results of this thesis show that freestanding graphene is robust enough to be used in future studies of laser plasma interaction. Adjustments need to be made to the existing target geometry to prevent an ionisation of the graphene-supporting structure. Based on the measured damage threshold, it is concluded, that, for future studies, the temporal laser pulse contrast needs to be improved, by reducing the amplified spontaneous emission of the laser.

Popular Science Summary

Particle accelerators are machines that generate beams of very fast moving particles. The particles can approach the speed of light and have large kinetic energy. Such particle beams are important for research in physics, biology, chemistry, and materials science. Industry also makes use of particle accelerators, and there are even applications in modern medicine for diagnostic and therapeutic purposes, for example for treating cancer.

The particles used in an accelerator are usually negatively charged electrons or positively charged ions. Together they form uncharged atoms, the building blocks of all matter around us. When isolated, however, the particles' charge allows them to be accelerated in electric fields. This is the mechanism all particle accelerators rely on.

The kinetic energy a particle can gain over a given distance is determined by the strength of the electric field. In conventional accelerators, the electric fields are confined in hollow metal structures, so called cavities. This limits the applicable field strengths, because extremely strong fields would damage the structure of the cavities themselves. The only way to increase the maximum energy of the particles is to build a longer accelerator. That is the reason why high energy particle accelerators are very big and expensive machines. The most famous example is the Large Hadron Collider (LHC), used for fundamental physics research at CERN close to Geneva, which has a circumference of 27 km and has cost several billion euros.

A technique called laser plasma acceleration is a new approach to this challenge. This mechanism eliminates the need for cavities, and hence also the technological limitation of the accelerating field strength. Instead the electric fields are generated in the interaction of a powerful laser pulse with a small amount of matter.

Modern high power laser systems can generate flashes of laser light with mind-boggling properties. The duration of these laser pulses can be as short as a few tens of femtoseconds. A femtosecond is a billionth of a millionth of a second, a timescale so short that even light can only travel a distance shorter than the diameter of a human hair. Such short pulses can reach a power of tens to thousands of terawatts. For comparison, the average power consumption of the entire world is roughly fifteen terawatts.

For laser plasma acceleration, these laser pulses are focused to a spot with a size of a few micrometres, comparable to the size of a bacterium. Concentrating such a high power on such a small area creates an ultra high intensity, exceeding 10^{18} Watts per square centimetre. Since light is an electromagnetic wave, this produces extremely strong electric fields. When such a focused pulse hits matter, it rips the constituting atoms apart. This creates a mixture of free electrons and ions, a so called plasma.

Under the right conditions, the laser pulse pushes the free electrons forward as an

ensemble, while the ions essentially stay at rest. Since the ions and electrons have opposite charges, there is a strong attractive force between them. This force accelerates the ions and makes them follow the electrons in their movement. The electric field between the electrons and the ions is several thousand times stronger than any field that can be generated in a conventional accelerator cavity. Therefore, the required acceleration length in a laser plasma accelerator is very short.

Laser plasma acceleration is a young research field and a lot of improvements are required, before it can be used for the applications mentioned above. One such optimisation concerns the target. If we want to accelerate ions, the target material for the laser pulse is usually a thin solid foil, and recently, it was motivated to consider new super-thin target materials.

In this thesis, it is investigated if it would be possible to use graphene as a target material. Graphene is the thinnest known material in the world. In its purest form it consists of a single layer of carbon atoms. Graphene has plenty of fascinating properties which have made it an extremely popular research subject during the last years. The thesis describes how it is possible to integrate graphene into laser plasma acceleration experiments. It also contains some interesting measurements that yield important information and leads for the next steps that should be taken in the development and research of graphene targets. One of these experiments, for example, served to determine at which laser intensity the graphene starts to show signs of damage, which helps to determine the required laser parameters. In this manner the stage is set for upcoming dedicated studies of this special material. It will be interesting to see where these investigations will lead, because there is hope that graphene targets may one day be used for the laser plasma acceleration of carbon ions, which would be immensely interesting for the particle therapy of difficult to reach tumours.

Abbreviations & Acronyms

ASE	Amplified Spontaneous Emission
CPA	Chirped Pulse Amplification
CR-39	Allyl Diglycol Carbonate
CSWA	Chirped Standing Wave Acceleration
CVD	Chemical Vapour Deposition
FWHM	Full Width Half Maximum
HeNe	Helium-neon
HOPG	Highly Oriented Pyrolytic Graphite
Nd:YAG	Neodymium-doped Yttrium Aluminium Garnet
PMMA	Poly(Methyl Methacrylate)
TEM	Transmission Electron Microscopy
Ti:sapphire	Titanium-doped Sapphire
TNSA	Target Normal Sheath Acceleration

Contents

1	Introduction	1
2	Laser Plasma Ion Acceleration	5
2.1	High Power Lasers	5
2.1.1	Gaussian Beams & Pulse Properties	6
2.1.2	Amplified Spontaneous Emission & Pulse Contrast	9
2.2	Laser Induced Ionisation	10
2.3	Plasmas	10
2.4	Laser Plasma Interaction	11
2.4.1	Ponderomotive Force	12
2.4.2	Relativistic Induced Transparency	13
2.5	Chirped Standing Wave Acceleration	14
3	Graphene	17
3.1	Graphene Properties	17
3.2	Fabrication of Suspended Graphene	19
3.3	Threshold for Laser Pulse Induced Damage	20
3.4	Raman Spectroscopy of Graphene	22
4	Experimental Setup	25
4.1	Lund Terawatt Laser	25
4.2	Experimental Chamber	26
4.2.1	Graphene Targets	29
4.2.2	Target Holder	29
4.3	Raman Spectroscopy for Diagnostic Purposes	31
4.4	Measuring the Laser Pulse Induced Damage Threshold	33
4.5	High Energy Shots on Graphene Targets	33
5	Results & Conclusion	35
5.1	Graphene Targets	35
5.2	Raman Spectroscopy	36
5.3	Laser Induced Damage Threshold	37
5.4	High Energy Shots	39
5.5	Conclusion	42
6	Outlook	43

Contents

Acknowledgements	45
References	47

1 Introduction

Particle accelerators are indispensable and widely used tools in modern research, industry, and applied medicine. Large scale research machines, like the Large Hadron Collider (LHC) at CERN or the newly installed MAX IV synchrotron facility in Lund, Sweden, are famous examples, but they only represent a small fraction of all accelerators found in today's world. High energy colliders, like the LHC, enable fundamental research in the field of high energy physics and are responsible for many discoveries, that helped shaping the current understanding of the world we live in on the fundamental level. At the same time, the radiation generated at synchrotron facilities provides unprecedented opportunities for structural research, providing new perspectives in physics, chemistry and biology. Additionally, many smaller accelerators can be found at universities, research centres, and in industrial environments, where particle beams support a broad range of experiments or production processes. Applications in the medical field include the production of short lived radioactive isotopes for diagnostic purposes and the generation of x-ray and ion beams for radiation treatment.

Conventional accelerators use cavities to contain the electric acceleration field, and this puts a limit on the energies they can achieve at a given size and cost. Typically charged particles get accelerated by a standing radio-frequency wave inside a resonant metal cavity. The energy a particle can gain over a given distance is limited to approximately 50 MeV/m. Electric breakdown would occur at higher accelerating field strengths and damage the walls of the accelerator. Hence, high energy accelerators are large and expensive machines, which are challenging to build and operate, even for large institutions. In order to significantly decrease the size and cost of future machines, a new, cavity-free acceleration mechanism needs to be developed. This would enable fundamental research at new energy frontiers, and also allow an increasing number of research institutions and hospitals to benefit from this technology.

With the development of high power laser systems, the exciting field of laser plasma acceleration has been opened. Modern laser systems, based on Chirped Pulse Amplification (CPA), generate ultra-short laser pulses, which can reach a peak power in the petawatt regime (10^{15} W). By focusing such a laser pulse to a spot size of just a few micrometres, intensities of up to 10^{21} W/cm² can be reached. When such an extreme pulse interacts with matter, the strong laser field ionises the atoms almost instantaneously and creates a plasma of free ions and electrons. Subsequently, the laser pulse interacts with the plasma and drives a collective motion of the lightweight electrons, while the heavier ions only respond very slowly and essentially stay at rest during the interaction. This behaviour results in a charge separation in the plasma and can lead to extremely strong electric

fields. Such a field is many orders of magnitude stronger than the maximum field in a conventional cavity, which leads to a significant reduction of the required acceleration length.

Laser plasma acceleration can be divided into two distinctly different fields. Electrons get accelerated with the help of a plasma wave, which is generated by a laser pulse traveling through an underdense plasma. This technique is called laser wakefield acceleration. Ion and proton acceleration, which this thesis will focus on, occur in overdense plasmas. The most common acceleration mechanism in this regime is target normal sheath acceleration (TNSA). In this process, protons and heavier ions can be accelerated to energies of several MeV over just a few micrometres, with the help of an electron sheath that generates extremely strong electric fields.

Laser-driven ion acceleration is subject to active research and development aiming to optimise the generated beams. So far the ion energies reached in laser plasma acceleration are too low for many applications. Other parameters that need to be optimised, before being able to complement conventional machines, are, for instance, the repetition rate and the stability of the beam. Another challenge is to understand, if and how one can chain up several acceleration stages to achieve higher energies than those of a single stage. Research during the last 15 years has greatly improved the understanding of ion acceleration mechanisms in overdense plasmas [1], but a lot of work remains to be done before the technology is ready for large scale applications.

Recently, an entirely new mechanism, named Chirped Standing Wave Acceleration (CSWA), has been proposed from within the PLIONA project¹ and demonstrated theoretically [2]. Simulations provide promising evidence, that CSWA will be able to overcome the energy limitations of TNSA and provide beams with an energy interesting for therapeutic purposes. At the same time it appears to be more stable than previously proposed alternative acceleration mechanisms.

For this concept, an ultra-thin foil is placed in front of a mirror with a spacing of half a laser wavelength. When a chirped and intense laser pulse is fired onto this assembly, the pulse is reflected by the mirror. A standing wave will build up in front of the mirror with the first node appearing at the location of the thin foil. The foil will have been transferred into the plasma state by the intense laser pulse at this point, and the electrons get trapped in the wave node due to the acting ponderomotive force. The chirp of the laser pulse is chosen such that the node moves away from the mirror, dragging the electrons along and creating the charge separation field that is needed to accelerate the ions.

One of the experimental challenges in implementing this novel method will be to find a material that is thin enough to transmit a majority of the laser pulse to the mirror, even after being fully ionised. A thick foil would provide a high density plasma at the surface upon laser incidence. This would reflect the laser pulse at the foil, instead of allowing a

¹The PLIONA (PLasma based ION Acceleration) project, financed by the Knut and Alice Wallenberg foundation, is a collaboration between researchers from Chalmers University, Gothenburg, Lund University, and Umeå University, devoted to explore and develop laser-driven ion acceleration theoretically and experimentally.

standing wave to be formed in front of the mirror. Further, the material has to withstand the laser long enough for the standing wave to build up. Otherwise the target layer gets blown up before the acceleration process begins.

Therefore, future experiments exploring CSWA, need to deal with a new class of ultra-thin target materials, and the use of graphene may be an interesting option in this context. Graphene, in its pure form, consists of only a single atomic layer of carbon; it is the thinnest solid target imaginable. In fact, graphene may be too thin for an efficient acceleration with established mechanisms. However, it is an interesting material for a future experimental implementation of CSWA. Single layer and multi-layer graphene are so thin that one can expect a significant amount of light to leak through the material. Even in the plasma state, high transmission is a likely scenario. These are good prerequisites for CSWA. In addition, graphene might turn out to be an interesting benchmark for existing theories, since it embodies the lower limit of solid target thickness.

Graphene is an interesting but challenging target material. It is usually produced and utilised as a thin film on the surface of a bulk substrate. For the purpose of laser plasma acceleration, however, freestanding graphene is required. Moreover, the suspended area has to be large enough for the laser to mainly interact with graphene instead of surrounding support material. Otherwise, the interaction of the laser pulse with the substrate would likely be the dominating effect in any experiment.

With the intention to prepare future experiments, this project is aimed at assessing the general viability of using graphene targets and gaining experience with their handling in the framework of laser plasma acceleration. The tasks include the design of suitable targets, as well as the development of techniques to mount, align, and diagnose the targets in the experiment. In addition to these preparatory steps, the threshold for laser induced damage of the graphene is measured. Lastly, high intensity shots are fired at the target, with the intention to look for traces of accelerated particles and to evaluate the resulting damage to the target structure. The results of this thesis will help to plan more complex experiments, further exploring the properties of this novel target material.

2 Laser Plasma Ion Acceleration

This thesis deals with graphene in the framework of laser plasma ion acceleration; the important concepts of this process are outlined in this chapter. Laser plasma acceleration is based on the interaction of ultra intense laser pulses with matter. In a typical ion or proton acceleration experiment, a short laser pulse is tightly focused onto a thin foil target. When the leading edge of the laser pulse hits the target, the material gets ionised almost instantaneously, due to the strong interactions between the atoms and the light field. In this manner, the target is transferred into the plasma state, where it no longer consists of neutral atoms, but can instead be described as a fluid consisting of free electrons and ions. These free charges are directly affected by the electromagnetic field of the laser pulse. Since electrons are significantly lighter than ions, they will respond to the external fields more rapidly and start moving, while the ions virtually stay at rest. The resulting electron displacement, relative to the ion background, can generate strong charge separation fields, which can be used for the acceleration of charged particles.

For a more accurate description of the acceleration process, it is necessary to introduce some core concepts and terminology. The first section of this chapter describes the generation and important properties of high intensity laser pulses. This is followed by an introduction to plasmas and the principles of laser plasma interaction. In the last section the newly proposed chirped standing wave acceleration will be explained.

2.1 High Power Lasers

Since their invention, lasers have become some of the most important tools of experimental physics, because they can be accurately controlled and generate well defined radiation, providing stable experimental conditions. While different lasers exist for a broad range of applications, all systems rely on a common principle; light gets coherently amplified by stimulated emission inside an optical gain medium. In order to provide energy to the laser, the medium is pumped, for example using flash lamps, other lasers, or electric discharges. The pumping results in a population inversion among the relevant electrons in the medium, meaning that the majority of them gets excited into a higher energy state. When photons from the laser beam interact with the medium, these electrons are stimulated to decay back into the lower state and emit new photons, with the same wavelength, direction, and phase as the incoming photons. The gain medium can be seen as an energy converter and determines the wavelength band that can be amplified in the laser.

High power lasers, like the Lund Terawatt Laser used in this project (see Section 4.1), accumulate a large amount of energy in very short pulses of light. For such a short pulse, the pulse duration becomes comparable to the oscillation period of light. Therefore a short pulse cannot be treated as a monochromatic wave, but has to be understood as a superposition of components within a band of frequencies or wavelengths. The shortest pulse duration, or Fourier transform limit, is given by [3]

$$\tau = \frac{0.44}{\Delta f} = \frac{0.44\lambda^2}{c\Delta\lambda}. \quad (2.1)$$

Here λ is the central laser wavelength, and c is the speed of light. Δf and $\Delta\lambda$ describe the width of the spectral distribution in terms of frequency and wavelength, respectively. A Gaussian shape in the temporal and frequency domain is assumed, and the pulse length and spectral width are given at Full Width Half Maximum (FWHM). The Lund Terawatt Laser, has a central wavelength 800 nm and reaches pulse durations of 35 fs, which corresponds to a bandwidth of roughly 27 nm. Hence, pulsed lasers require a gain medium with broadband amplification. Titanium-doped sapphire (Ti:sapphire) offers amplification across a very broad band, and additionally has a very high damage threshold. Thus, it has become the standard gain medium in tabletop short pulse systems.

It is practically impossible to generate high energy pulses within a single closed laser cavity. Therefore, the established technique is to generate lower power pulses in a classical oscillator setup, and subsequently amplify these pulses in several stages. All these stages have an individually pumped gain medium, through which the pulse is guided, in order to collect more and more energy.

Generating high power pulses is challenging, because the beam quickly reaches intensity levels that are high enough to burn the gain medium. A pulse energy of 1 J at a pulse duration of 50 fs, for example, corresponds to a power of approximately 20 TW (cf. Equation 2.6). One solution is to expand the beam, such that the power is spread out over a larger cross section area, and the intensity is thus reduced. In practice, however, the maximum beam size is usually limited to a few centimetres, due to the high price of larger optical elements. Instead, it is significantly more efficient to stretch the pulse in the time domain and reduce the power. By using dispersive elements to introduce a wavelength dependent delay, the pulse can be stretched over several picoseconds. This reduces the power and intensity by more than four orders of magnitude, without the need for larger optics. Once the pulse is fully amplified, it can be re-compressed in time to reach the maximum power. This method is called Chirped Pulse Amplification (CPA) [4]. CPA can be combined with a gradual beam expansion, where the beam size is adjusted to the increasing energy along the amplification chain.

2.1.1 Gaussian Beams & Pulse Properties

Continuous, monochromatic laser beams can be mathematically modelled as so called Gaussian beams. This description is not entirely correct for short, polychromatic pulses,

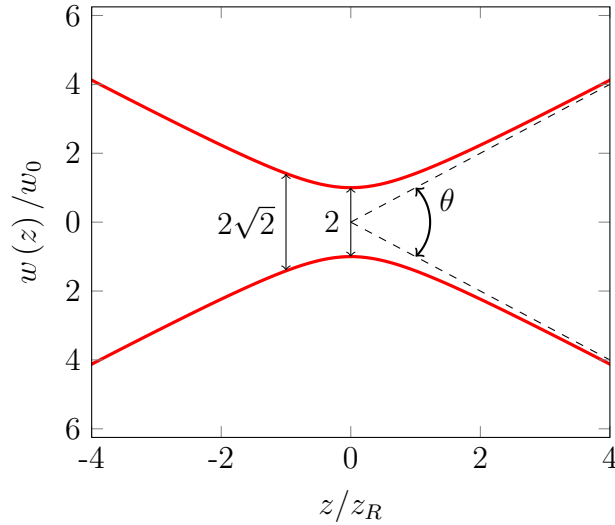


Figure 2.1: The figure shows the waist of a Gaussian beam. It has a waist diameter $2w_0$ and diverges with an angle θ . One Rayleigh range z_R away from the waist the beam has expanded by a factor $\sqrt{2}$. With permission from K. Svensson [5].

but it works as a good approximation. In order to calculate important pulse parameters, the essential components of the Gaussian beam model are presented here.

For the following derivations a round, paraxial laser beam with linear polarisation is assumed; it propagates along the z -axis and the distance from the beam axis is denoted with ρ . In Gaussian beam optics, the electric field of the laser is given by a complex Gaussian function $\mathbf{E}(t, \rho, z)$, oscillating over time, t . This function confines the electric field around the beam axis, which provides a more accurate description of a laser beam than a conventional plane wave. At any point z along the beam, the transverse intensity profile I has the shape of a Gaussian distribution

$$I(\rho, z) \propto \exp\left(\frac{-2\rho^2}{w^2(z)}\right). \quad (2.2)$$

The beam radius $w(z)$ is the distance from the beam axis where the intensity has dropped by a factor $e^{-2} \approx 0.13$; it encloses approximately 86% of the total beam energy. In practice, the beam width is often measured in terms of the FWHM, which can be translated into the beam radius as $w = w_{\text{FWHM}}/\sqrt{2 \ln 2} \approx 0.85 w_{\text{FWHM}}$.

In a laser plasma acceleration experiment, the highest intensities are reached by focusing the high power laser onto the target. Suppose a Gaussian beam with wavelength λ is loosely focused to a spot with minimum radius w_0 at position $z = 0$, see Figure 2.1. Under these conditions the beam diverges with an angle $\theta = 2\lambda/\pi w_0$. Due to the divergence, the beam radius increases as one moves away from the waist. At any point around the

beam waist, the radius of the beam is given as

$$w(z) = w_0 \sqrt{1 + \left(\frac{z}{z_R}\right)^2}. \quad (2.3)$$

Here z_R is the so called Rayleigh range. It is a measure for the length of the beam waist and defined by

$$z_R = \frac{\pi w_0^2}{\lambda}. \quad (2.4)$$

Since the beam intensity is inversely proportional to the beam cross section, it decreases as $I \propto (w_0/w(z))^2$ when leaving the focus. At $z = \pm z_R$ the intensity falls to 50% of its peak value.

The laser beam is not continuous. Therefore it is necessary to introduce an envelope function which defines the temporal profile of the pulse. A Gaussian pulse shape, with FWHM pulse duration τ , is defined by

$$I(t, z) \propto \exp\left(-4 \ln 2 \frac{(t - z/c)^2}{\tau^2}\right). \quad (2.5)$$

This definition does not account for a chirped pulses, because they are usually compressed to minimum length and considered chirp-free before entering the experiment. For a pulse with total energy E_p the peak power of the pulse is

$$P_0 = 2 \sqrt{\frac{\ln 2}{\pi}} \frac{E_p}{\tau} \approx 0.94 \frac{E_p}{\tau}. \quad (2.6)$$

Having introduced the important components of the model, the full description for the intensity distribution of a Gaussian laser pulse can be written as

$$I(t, \rho, z) = I_0 \left(\frac{w_0}{w(z)}\right)^2 \exp\left(\frac{-2\rho^2}{w^2(z)}\right) \exp\left(-4 \ln 2 \frac{(t - z/c)^2}{\tau^2}\right). \quad (2.7)$$

Intuitively, the peak intensity depends on the peak power and the focal cross section

$$I_0 = \frac{2P_0}{\pi w_0^2}. \quad (2.8)$$

As will become clear later, another figure of interest is the fluence, F , which denotes the integrated energy flux for a single pulse. The peak fluence is given by

$$F_0 = \frac{2E_p}{\pi w_0^2}. \quad (2.9)$$

Now it is possible to estimate characteristic experimental parameters. After compression, pulses from the Lund Terawatt Laser normally carry an energy of $E_p = 0.8$ J at a pulse length of $\tau = 40$ fs. For ion acceleration experiments the focal spot radius is typically $w_{0,\text{FWHM}} = 5$ μm . Hence, the peak intensity is $I_0 \approx 7 \times 10^{19}$ W/cm².

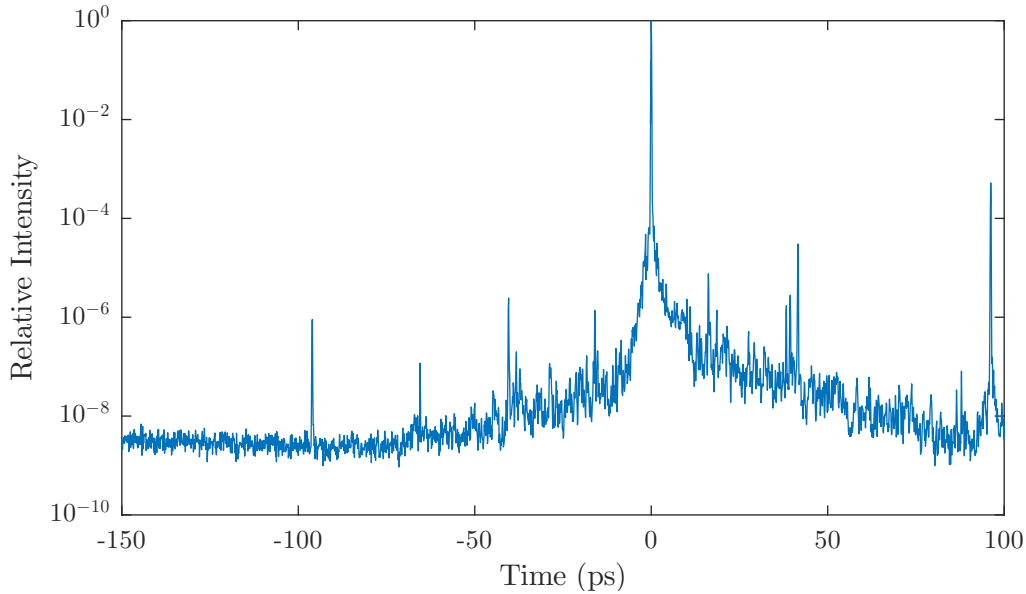


Figure 2.2: The plot shows a typical pulse contrast measurement. The contrast of the ASE pedestal is approximately 3.4×10^{-9} . Besides the pedestal a few pre-pulses can be seen in the scan; they may, however, be artifacts of the very sensitive measurement.

2.1.2 Amplified Spontaneous Emission & Pulse Contrast

In practice, the pulses in a high power laser system are surrounded by a significant level of background noise. As discussed above, the pulses are generated in a chain of several amplification stages. Spontaneous emission occurs in the gain medium of each of these amplifiers and produces photons that are not correlated to the main pulse. When such photons get emitted in the forward beam direction and temporally close to the main pulse, they can be amplified themselves further downstream. This is called Amplified Spontaneous Emission (ASE). Due to this effect, a high power femtosecond pulse is generally sitting on top of an ASE pedestal, with a duration of a couple of nanoseconds. The pedestal is usually many orders of magnitude weaker than the main pulse, but when focused, it can still reach significant intensities of $\gtrsim \text{GW}/\text{cm}^2$. Due to the nanosecond scale duration of the ASE, this corresponds to an ASE related fluence of $\gtrsim \text{J}/\text{cm}^2$. Therefore the ASE can heat and damage the target before the main pulse arrives. Especially when working with very thin targets, this is problematic, because it decreases the efficiency of the acceleration process.

The strength of the ASE pedestal is usually expressed relative to the peak power of the pulse, defining the so called pulse contrast. Figure 2.2 shows a contrast measurement from the Lund Terawatt Laser. Up until tens of picoseconds before the main pulse, the ASE is fairly constant, with a contrast of typically 10^{-9} ; then the intensity rapidly increases by many orders of magnitude and ultimately spikes at the main pulse.

One way to improve the pulse contrast is to use a plasma mirror [6]. The pulse gets

reflected by a self induced plasma on the surface of a transparent glass plate. Before the plasma formation, the leading pedestal gets transmitted through the glass. Hence, a plasma mirror filters out a significant fraction of the ASE. However, the experimental implementation of a plasma mirror is complex and was not a part of this project.

2.2 Laser Induced Ionisation

In an ion or proton acceleration experiment, the laser pulse is focused onto a solid target, usually a thin foil with a thickness of a few μm . At the high intensities found in laser plasma experiments, the target material gets ionised almost instantaneously. This is possible, because the electric field strength of the laser pulse is comparable to the field strength inside the target atoms. In the presence of a powerful laser pulse, the Coulomb potential of an atom gets perturbed so strongly that the maximum value of the potential barrier gets pushed below the electron binding energy. At this point the electrons are no longer trapped and escape from the atom. It can be shown, that for free atoms or ions the intensity threshold for “over the barrier ionisation” is given by

$$I_{OBI} = \frac{c\epsilon_0^3\pi^2 E_{ion}^4}{2Z^2 q_e^6} \approx 4 \times 10^9 \text{ W/cm}^2 \cdot \frac{(E_{ion}/\text{eV})^4}{Z^2}, \quad (2.10)$$

where Z is the charge number of the produced ion, ϵ_0 the electric constant, q_e the elementary charge, and E_{ion} denotes the ionisation energy associated with the released electron [7]. Hydrogen, which is commonly adsorbed on the target surface, has an ionisation energy of 13.6 eV. This corresponds to an ionisation intensity of $1.4 \times 10^{14} \text{ W/cm}^2$. For carbon the threshold ranges from $6.4 \times 10^{13} \text{ W/cm}^2$ for the production of C^{1+} to $6.4 \times 10^{18} \text{ W/cm}^2$ for fully ionised C^{6+} . These thresholds are smaller than typical peak intensities in ion acceleration schemes $\gtrsim 10^{19} \text{ W/cm}^2$. Hence, carbon, and consequently graphene, will be fully ionised before the laser pulse reaches its peak intensity. This means that all electrons contribute to the plasma electron density.

However, it is important to note that the threshold intensity is derived for free atoms. In a solid target the interactions with short pulses are far more complex, and ionisation can occur at significantly lower intensities. Possible effects include electric breakdown and avalanche ionisation, where free electrons ionise further atoms. The fluence is often a better measure for the onset of laser induced damage in this case. As will be presented in Section 3.3, the threshold fluence of graphene is 200 mJ/cm^2 for nanosecond pulses [8]. Since, as explained in the previous section, the ASE fluence can reach several J/cm^2 it becomes clear that the target is damaged a long time before the arrival of the pulse peak.

2.3 Plasmas

Due to the ionisation of the target during the early stages of interaction with the laser, the peak of the pulse will never interact with conventional matter, but with a mixture

of free electrons and ions. The target material is said to be in the plasma state. In this extreme state, matter is described as a fluid of free charges which is governed by collective effects. The full description of plasma dynamics is complex and beyond the scope of this report. However, two important quantities will be introduced here, as they are essential to understand laser plasma interactions.

An important property of plasma is quasi-neutrality. The high mobility of plasma electrons allows them to rearrange quickly and shield local charge imbalances. Hence a plasma appears neutral on large scales. The characteristic length required for effective shielding is the so called Debye length

$$\lambda_D = \sqrt{\frac{\epsilon_0 k_B T_e}{q_e^2 n_e}}, \quad (2.11)$$

where k_B is Boltzmann constant, T_e the electron temperature, and n_e denotes the plasma electron density [9]. Although the plasma response to perturbations is fast, the Debye-shielding is not built up instantaneously. The characteristic timescale for the electron rearrangement is $\tau_P = \lambda_D/v_e$, where the electron velocity can be approximated with the thermal velocity $v_e = \sqrt{k_B T_e/m_e}$, with electron mass m_e . This timescale defines the plasma frequency

$$\omega_p = \frac{1}{\tau_P} = \sqrt{\frac{q_e^2 n_e}{\epsilon_0 m_e}}. \quad (2.12)$$

Also called Langmuir frequency, this is the characteristic frequency for plasma oscillations [9]. The meaning of this frequency for laser plasma interactions will become clear in the next section.

It should be mentioned that concerns can be raised, about whether graphene, with its sub-nanometre thickness, can be accurately described as a plasma after ionisation. At moderate electron temperatures, equivalent to 1 keV, the Debye length becomes comparable to the graphene thickness. In this scenario, the plasma may not respond to external perturbations in the usual way. This formal problem obviously arises, because graphene is essentially a two dimensional material, while plasma theory is developed in three dimensions. On the other hand, solid targets generally expand due to heating and develop a plasma with a density gradient. Therefore, ionised graphene can probably be seen as a volumetric plasma with a density gradient. An answer to this issue is not provided in this report, but it may be important to consider in the future.

2.4 Laser Plasma Interaction

Since the free charges in a plasma are directly affected by the electromagnetic field of the laser pulse, laser plasma interactions are fundamentally different from low intensity light matter interactions. The propagation of laser pulses in a plasma is determined by the dispersion relation. For the derivation of the dispersion relation, it is assumed that the ions are stationary, because they are too heavy to follow the rapid oscillations of the light

field. In front of this ion background, the electric field of the laser, \mathbf{E} , induces electron displacement currents. This leads to the following differential equation for the electric field

$$\nabla^2 \mathbf{E} - \nabla(\nabla \cdot \mathbf{E}) + \frac{\omega^2}{c^2} \left(1 - \frac{\omega_p^2}{\omega^2}\right) \mathbf{E} = 0, \quad (2.13)$$

which is solved by a plane wave $\mathbf{E} = E \exp(i(\mathbf{k}\mathbf{r} - \omega t))$ and yields

$$\omega^2 = \omega_p^2 + k^2 c^2. \quad (2.14)$$

Here ω_p is the characteristic plasma frequency, as defined in Equation 2.12. The light angular frequency and wave vector are denoted with ω and k , respectively. The essential conclusion from the dispersion relation is, that light with a frequency $\omega < \omega_p$ cannot propagate in the plasma. For light of such frequencies the plasma response is fast enough to cancel the incoming radiation entirely. The electrons screen the light field, and the laser gets reflected by the plasma.

In practice, the laser frequency is determined by the laser system and cannot be changed. Therefore, it is useful to define the critical density

$$n_c = \frac{\epsilon_0 m_e \omega^2}{q_e^2} = \frac{4\pi^2 \epsilon_0 m_e c^2}{q_e^2 \lambda^2}. \quad (2.15)$$

This is the electron density, above which a laser with wavelength λ gets reflected by a plasma. If the actual density of a plasma lies below the critical density it is called underdense; a plasma with higher electron density is referred to as overdense.

For the Lund Terawatt Laser $\lambda = 800 \text{ nm}$, and the critical electron density is $n_c = 1.74 \times 10^{21} \text{ cm}^{-3}$ accordingly. Because the electron density in solid targets is usually on the order of 10^{23} to 10^{24} cm^{-3} , the resulting plasma is overdense and impenetrable for the laser pulse. Since the plasma quickly expands from its initial position, the peak of the laser pulse usually sees an increasing plasma density gradient. It can propagate into the plasma, until it reaches the critical density threshold where it gets reflected.

Important plasma heating processes take place at this barrier. When the laser is obliquely incident, it gets refracted in the plasma gradient and reflected before reaching the critical density surface. If the laser is polarised nonparallel to this surface, the ponderomotive force (explained below) can accelerate electrons and drive them through the critical density surface. This heats the volume of the plasma and can enhance the acceleration.

2.4.1 Ponderomotive Force

The ponderomotive force is one of the most important forces in the field of high intensity light matter interactions. It describes the net force on a charged particle inside an oscillating electromagnetic field. Finding a fully relativistic expression of the ponderomotive

force is difficult, but the essential dependencies are

$$\mathbf{F}_{pond} \propto -\frac{q^2}{m} \nabla I. \quad (2.16)$$

This is the average force over a full oscillation period of the electromagnetic field, and it shows that particles of charge q are pushed away from regions of high intensity. Important to note is, that the force is independent of the sign of the charge, and hence pushes electrons and ions in the same direction. However, the mass dependency implies, that the effect on ions can be neglected relative to the effect on electrons.

The pondermotive force can be explained in the following way. In the electric field of an electromagnetic wave, a free charged particle will perform a wiggling motion, perpendicular to the propagation direction of the wave. For a plane wave, this would not have a net effect on the position of the particle, as it would just oscillate around its equilibrium position. The situation is entirely different in the focus of a Gaussian beam, where the electric field strength varies strongly with the distance from the laser axis. As the charged particle gets accelerated from the centre towards the edge of the beam, the amplitude of the electric field decreases. Therefore, on the way back, the restoring force is smaller, and the particle will not completely return to its initial position. As this oscillation continues, the charged particle effectively drifts away from the region of high intensity in the transverse direction and can gain a net transverse momentum.

For ultra high intensity laser pulses, electrons can reach relativistic velocities, \mathbf{v} , during the transverse ponderomotive oscillation. Suddenly, the magnetic component of the Lorentz force $\propto \mathbf{v} \times \mathbf{B}$ has a significant contribution. The transverse motion of the electron will couple to the magnetic field, \mathbf{B} , of the laser, and result in an additional longitudinal translation. Once again, there should be no net gain of longitudinal momentum. Yet, since the particle drifts towards the edge of the beam during the longitudinal push, the decelerating field will be weaker than the accelerating field, generating a net longitudinal momentum of the electron.

2.4.2 Relativistic Induced Transparency

Relativistic effects also have an influence on the plasma opacity. As explained in Section 2.4 a plasma is opaque to the laser pulse, if its electron density n_e is larger than the critical density n_c . This condition changes in a relativistic plasma. When electrons get accelerated to velocities close to the speed of light, they experience a relativistic mass increase $m_e \rightarrow \gamma m_e$, where $\gamma = 1/\sqrt{1 - (v/c)^2}$ is the relativistic gamma factor. The electron trajectories get more rigid, which reduces the ability of the plasma to respond to high frequency external fields. Therefore the effective plasma frequency decreases, $\omega_p \rightarrow \omega_p/\sqrt{\gamma}$. Once a plasma fulfils the condition that $n_e \leq \gamma n_c$, it becomes transparent to the laser pulse. This regime is called relativistic induced transparency or self induced transparency.

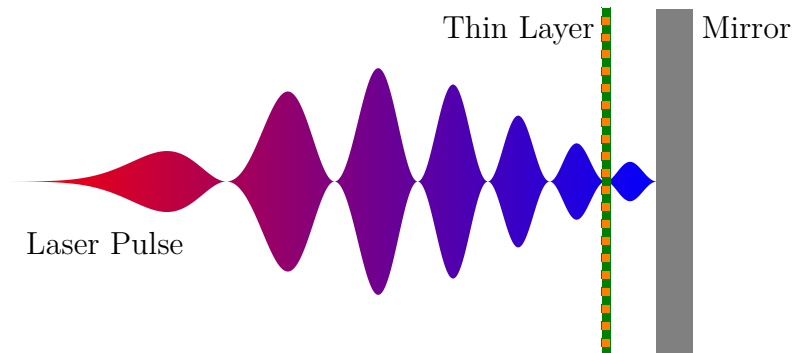
In practice this effect is mainly of interest for thin solid targets. As soon as the target gets ionised, the resulting plasma will start to expand, which reduces the electron density. Usually this expansion is too slow to reduce the plasma density below the critical threshold before the peak of the laser pulse arrives. For $\gamma \gg 1$, however, expansion and relativistic effects combined, can reach the self induced transparency regime, allowing the laser pulse to propagate into and through the plasma. This leads to an interaction between the volume of the plasma and the laser pulse, which would normally be reflected by the electrons at the critical density surface. The consequences of relativistic induced transparency for laser plasma acceleration are subject to ongoing research [10–12]. Further it is an important prerequisite for successful chirped standing wave acceleration, which will be explained in the next section.

2.5 Chirped Standing Wave Acceleration

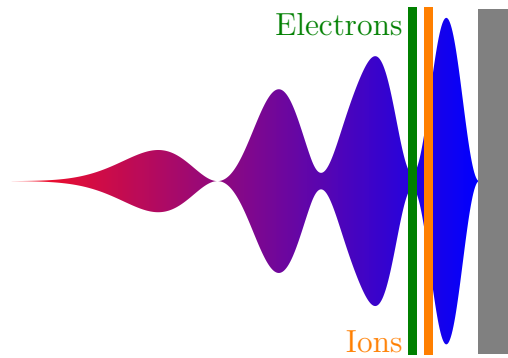
In the past, a number of different mechanisms for laser plasma acceleration of ions have been discovered. The majority of these mechanisms is using the electrons as a mediator to transfer energy from the laser pulse to the ions. Since the electrons have a higher charge to mass ratio than the ions, the ponderomotive force acting on them is larger, and their inertia is smaller; in total the acceleration of a charged particle due to the ponderomotive force scales as $a \propto m^{-2}$. Hence the electrons get accelerated, while the ions essentially remain stationary. This collective electron movement, relative to the ion background, generates a global charge displacement in the plasma. In this situation, the ions experience a strong attraction towards the escaping electrons and get dragged along. Controlling and optimising this conversion process is the core interest of current research on laser plasma acceleration. A detailed review of the progress in this field can be found in [1]. A novel approach for the electron mediated acceleration of ions was proposed recently and will be presented below.

Chirped Standing Wave Acceleration (CSWA) [2] was developed to overcome the limitations of established laser plasma acceleration mechanisms. These existing mechanisms either show inconvenient scaling laws, meaning that the laser power needs to be increased drastically to achieve particle energies interesting for most applications, or they are prone to instabilities, which makes their experimental implementation difficult and limits the maximum energy. The common problem of the aforementioned acceleration schemes is the lack of control over the escaping electrons. Since the electrons move with velocities close to the speed of light, there is only a very short time frame for efficient ion acceleration. Due to their high mass the ions move at significantly lower velocities and cannot keep up with the electrons. As the distance between both species increases the accelerating field gets weaker. The main idea of CSWA is to gain control over the escaping electron population and to match their velocity to the accelerating ions. In this way the efficiency of the acceleration process can be improved.

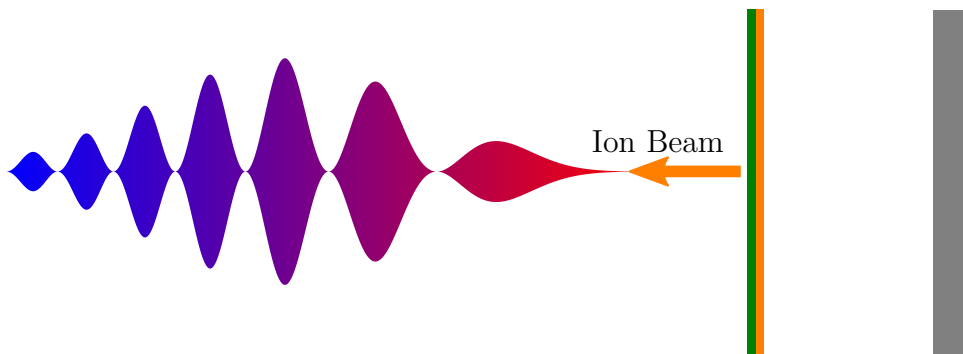
CSWA is based on trapping the electrons in the ponderomotive potential of a standing



(a) The chirped laser pulse gets transmitted through the thin plasma layer and will form a standing wave, upon reflection from the mirror, with a node at the location of the plasma.



(b) The electrons are trapped in the ponderomotive potential and get dragged along as the wave node moves forward, due to the pulse chirp. This creates the needed electric field for the acceleration of the plasma ions.



(c) After the acceleration process, the electrons, ions, and the laser pulse propagate away from the target assembly.

Figure 2.3: Visualisation of the CSWA process, based on [2].

wave, see Figure 2.3. For this purpose the CSWA target contains two elements, a mirror and an ultra thin foil. These components are separated by a distance that is a small multiple of half the laser wavelength, e.g. $\lambda/2$ or λ . The laser pulses proposed for CSWA are circularly polarised, and they have a down-chirp, which means that the wavelength increases with time. When the laser pulse arrives at the target assembly, it ionises the foil but gets transmitted through the plasma due to relativistic transparency. Upon reflection from the mirror, the pulse forms a standing wave, and due to the chosen spacing, a node will appear at the location of the foil. This means that the plasma is trapped in the ponderomotive potential of the neighbouring anti-nodes. Due to the down-chirp of the pulse, the node moves away from the mirror and the ponderomotive force pulls the trapped electrons along. This creates the needed charge separation for the acceleration of plasma ions. The key trick is that the chirp of the pulse can be matched to the acceleration rate of the ions. In this way, a strong charge separation field can be maintained for an extended time, because the electrons do not run off in an uncontrolled fashion.

So far CSWA has been demonstrated successfully only in simulations. An experimental implementation of this mechanism is not trivial. One of the main challenges will be the development of a suitable target assembly. It is essential, that the thin foil quickly becomes relativistically transparent upon arrival of the laser pulse. Otherwise the pulse gets reflected by the plasma, which will push the foil forward into the mirror, instead of accelerating the ions in the backward direction. This will certainly require a very thin, but stable target material. It should be investigated if graphene may be a suitable material for this purpose. Investigating the development of CSWA targets is therefore one of the main drivers behind this master thesis.

3 Graphene

Throughout this project, considerable effort has been devoted to gathering information on graphene. Since graphene is a novel material in the context of laser plasma acceleration, there was no prior experience with such targets. This chapter summarises the most important results of the literature search, which was conducted in order to learn about the handling of graphene. In the first section the basic material properties of graphene are introduced. The graphene samples for this project were produced externally, but in the future targets may be fabricated in-house. An overview of possible manufacturing processes is therefore presented in the second section. This is followed by a discussion of the threshold for laser induced damage, because graphene, being an ultra-thin material, is expected to be heavily affected by the ASE pedestal of the laser pulse, unless extra precautions are taken. The final section of this chapter deals with Raman spectroscopy, which may be used for diagnostic purposes in the future.

3.1 Graphene Properties

Graphene is an ultra-thin, two-dimensional sheet of material that consists of a single atomic layer of carbon; it is the fundamental building block of more complex carbon allotropes, like graphite, nanotubes, and fullerenes. Graphite is formed by a large number of stacked graphene layers that are weakly bound by van der Waals forces. Since the forces between individual layers are much weaker than the intra-sheet forces, they can be separated and sheared against each other with little force, and without damaging the constituting sheets. It was widely deemed impossible to isolate graphene sheets in practice, until Novoselov *et al.* reported the successful production of graphene, using the micromechanical cleavage method, in 2004 [13]. In this process, a thin graphite sheet is exfoliated from a highly oriented pyrolytic graphite (HOPG) crystal. Afterwards the layers of this sheet are repeatedly peeled apart using adhesive tape, until only a single layer of graphene remains. While the term graphene strictly speaking defines a single layer, it is also commonly used for multi-layer graphene with up to tens of layers.

The crystal structure of graphene is formed by a flat honeycomb lattice, where each carbon atom forms covalent bonds with three neighbouring atoms, see Figure 3.1. The distance between neighbouring atoms is $a = 1.42 \text{ \AA}$. Measuring the thickness of graphene is not trivial, and the method has a significant influence on the result. Yet, an intuitive choice is to define the thickness by means of the layer spacing in graphite, $d = 3.35 \text{ \AA}$. Accurate atomic force microscopy confirms that this is a good reference value [14].

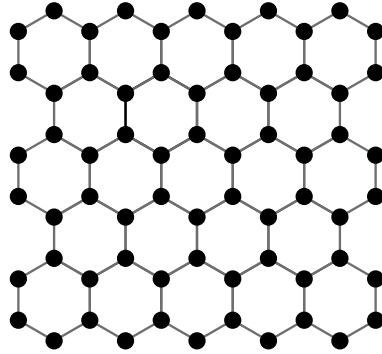


Figure 3.1: The carbon atoms in a graphene layer are arranged in a honeycomb lattice with an internuclear distance of 1.42 \AA .

With this information, it is possible to calculate the electron density of graphene. For laser plasma acceleration, this value is of interest, because it can be used to estimate the generated plasma density. As was discussed in Section 2.4, the plasma density characterises the interaction with the laser pulse. Considering that each honeycomb cell contains two carbon atoms, with six electrons each, the electron areal density of single layer graphene (SLG) can be computed:

$$n_{SLG}^A = \frac{2 \cdot 6}{A} \approx 2.29 \times 10^{16} \text{ cm}^{-2}. \quad (3.1)$$

Here $A = 3\sqrt{3}/2 \cdot a^2 \approx 5.24 \text{ \AA}^2$ is the area of a single cell. For multi-layer graphene (MLG), the integrated electron areal density is simply given as $n_{MLG}^A = N_L n_{SLG}^A$, where N_L is the number of layers. Using the layer thickness as defined above, the volumetric electron density follows as

$$n_G^V = \frac{n_{SLG}^A}{d} \approx 6.84 \times 10^{23} \text{ cm}^{-3}. \quad (3.2)$$

This is a handy value in order to compare the electron density of multi-layer graphene to existing thin target materials, like nanometre scale diamond-like carbon $n_{DLC} \approx 9 \times 10^{23} \text{ cm}^{-3}$ or aluminium $n_{Al} \approx 7.8 \times 10^{23} \text{ cm}^{-3}$.

For experimental purposes, it is also practical to take note of the basic optical properties of freestanding graphene. As a two-dimensional material, graphene displays some surprising properties and offers plenty of opportunities for accurate theoretical modelling. Such theoretical work arrived at the conclusion, that the white light transmittance of single layer graphene

$$T_{SLG} = \left(1 + \frac{\pi\alpha}{2}\right)^{-2} \approx 97.7\% \quad (3.3)$$

only depends on the fine structure constant $\alpha \approx 1/137$ [15]. The corresponding reflectance is [16]

$$R_{SLG} = \frac{\pi^2 \alpha^2 T}{4} \approx 0.01\%. \quad (3.4)$$

Experiments on suspended graphene [16] have not only confirmed the white light transmittance for a single layer, but further demonstrated that the opacity, κ , of graphene films scales linearly with the number of layers for few-layer systems,

$$\kappa_{MLG} = N_L(1 - T_{SLG}) \approx 2.3\% \cdot N_L. \quad (3.5)$$

The single layer reflectance was reported to be well below 0.1% in the same study. Due to the relatively strong absorption of even a single layer, it is possible to observe graphene films directly in transmission. Large flakes can even be seen with the bare eye. This makes the observation and alignment of freestanding graphene targets a straightforward process, as is shown in Section 4.2.

3.2 Fabrication of Suspended Graphene

Nowadays the fabrication of graphene is widely based on Chemical Vapour Deposition (CVD), because the micromechanical cleavage method is not suitable for large scale production. The cleavage method usually limits the size of continuous graphene films to a few micrometres. In the established CVD growth procedures, a metal surface is exposed to small amounts of carbon donor molecules in a high temperature environment. Methane is commonly used as a donor. The donor molecules dissociate at the metal surface, depositing carbon atoms on the substrate. Once cooled down, a graphene film covers the metal surface. The specific growth mechanism and the properties of the graphene film depend on the substrate and parameters like the temperature and gas flow. Copper foils have turned out to be a reliable growth substrate for single layer graphene [17], while nickel substrates provide multi-layer graphene, with typically up to ten layers [18]. Developing and optimising the CVD growth procedure is still subject to active research. Nevertheless, CVD can already reliably produce continuous graphene films covering several square centimetres. CVD grown graphene is now widely commercially available and can be acquired for further individual processing.

The challenge in manufacturing a graphene target for a laser plasma experiment is the need to use freestanding graphene. The sheet needs to be directly accessible from both sides; hence it cannot be supported by a substrate. Since graphene cannot be grown across large substrate gaps yet, multiple processing steps are needed to fabricate free standing membranes. For this purpose the CVD graphene is either transferred onto another structured substrate or parts of the growth substrate are chemically removed without damaging the graphene film.

A well established method to move graphene from one substrate to another is the PMMA transfer [19]. In the first step of this process, the graphene is spin-coated with a thin layer of poly(methyl methacrylate), also known as PMMA or acrylic glass. When the coating has hardened, the substrate is wetted or carefully etched until the PMMA/-graphene stack starts to peel off. The stack can be manually transferred onto the new substrate, where van der Waals forces will cause it to attach to the new surface. In the

final step, the PMMA layer is dissolved with acetone, such that only the graphene remains on the new substrate.

This transfer method can be used with a holey substrate in order to produce free-standing membranes. Without careful adjustments though, the size of such membranes is limited to a few tens of microns, because surface tension forces between the solvent and the graphene lead to rupture of the membrane during the drying of the sample. Recently, however, five-layer graphene was successfully suspended over circular apertures with a 1.5 mm diameter. This was achieved by optimising the transfer procedure and continually replacing the PMMA-solvent with a low surface tension liquid before allowing the membrane to dry [20]. It is worth mentioning, that these five atomic layer thick membranes were able to withstand a remarkable pressure difference of up to 1800 Pa.

Instead of using a carrier material like PMMA, the graphene can also be transferred directly between substrate materials. The PMMA transfer involves many steps and often requires subsequent cleaning procedures, too, because small amounts of PMMA and solvent remain on the graphene. In order to simplify the transfer and bypass the pollution of the graphene, the direct transfer method was developed [21]. Instead of using a coating, the new substrate is brought into direct contact with the graphene. To bind the graphene to the new substrate, it is wetted with isopropanol. When the isopropanol evaporates, surface tension pulls the the new substrate towards the graphene and assists in generating a strong adhesion between the two materials. Now the old substrate can be etched off, and in this manner the graphene gets isolated on the new substrate. This procedure has been successfully demonstrated for single and multi-layer transfers onto holey substrates. Yet, since both substrates get immersed in the same etchant, the direct transfer method cannot be used for transfers between substrates made of the same material.

An alternative to the graphene transfer is to directly treat the growth substrate with lithographic methods [22]. First the graphene/substrate stack is coated with photoresist on all sides. The resist serves to protect the substrate from an etchant. In the next step a photomask is imaged onto the back side of the substrate with UV light to define the etching pattern. After the development of the photoresist, certain areas of the substrate back side are exposed, while the front surface and the graphene are still protected by resist. The exposed areas get etched through the entire substrate thickness, leaving only the inert graphene film on the front side. Afterwards the photo resist is removed, and the patterned substrate with the now suspended graphene remains. An interesting feature of this fabrication process is its scalability. All the steps are based on established lithography procedures and appear to be fit for automation.

3.3 Threshold for Laser Pulse Induced Damage

When considering high intensity experiments on thin films, it is important to consider the threshold for laser pulse induced damage to the material. As explained in Section 2.1.2, the main laser pulse (\sim fs) is preceded by the ASE pedestal (\sim ns) and its own rising edge

(\sim ps). For a successful acceleration process, the target material must not be evaporated before the main pulse arrives. The ASE pedestal can drive a significant heating, melting, and expansion of the target a long time before that; this is a limiting factor for thin targets in general and would also concern CSWA. In order to plan experiments on graphene targets, it is necessary to understand how the material will respond to the energy deposited before the arrival of the main pulse. Thus the threshold for laser induced damage is of high interest.

Laser ablation of graphene has been investigated widely, and a threshold fluence of approximately 200 mJ/cm^2 is consistently reported [8, 23–25]. However, so far experiments have almost exclusively been performed on substrate-supported graphene. The substrate can be expected to act as a heat sink and provide additional mechanical stability to the graphene. Therefore the damage threshold for freestanding graphene should be determined independently. Such a measurement is part of this thesis and presented in Sections 4.4 and 5.3.

Existing studies contain highly interesting and relevant information about the ablation of graphene films with high intensity laser pulses. The most important results are presented here in the form of a short summary.

In 2001, before the actual discovery of graphene, Jeschke *et al.* performed simulations of thin graphite films, essentially multi-layer graphene, and identified two laser ablation mechanisms [25]. Simulating 20 fs laser pulses, they found, that at a threshold fluence of 290 mJ/cm^2 , the intra-layer carbon bonds break up and the structure gets strongly distorted. This concludes in single atom evaporation of the film. At a slightly lower value of 170 mJ/cm^2 though, the pulse launches a compression wave into the layer stack. The wave results in layer collisions and the subsequent ejection of surface layers. Significant intra-layer damage is not observed in this case. Both ablation mechanisms play out within tens to hundreds of femtoseconds after the pulse hits the graphite.

Experiments have confirmed the theoretical prediction of the threshold fluence with reasonable agreement. A striking result is that, for laser pulse durations ranging over 5 orders of magnitude from 50 fs up to 5 ns, the ablation of single layer graphene is consistently observed at a peak fluence of approximately 200 mJ/cm^2 [8, 23, 24]. Thus, it seems that on all these timescales, the damage threshold is not defined by the laser intensity, but by the fluence, which indicates a limit on the speed of the heat dissipation in the graphene film. Almost all of these measurements are performed on various substrates, like glass, sapphire, silicon, and silicon oxide. Yoo *et al.*, however, performed a comparative measurement on freestanding graphene and also observed ablation at a lower peak fluence $\sim 80 \text{ mJ/cm}^2$ for 100 fs pulses [24]. This supports the assumption that a substrate stabilises the graphene and motivates an independent measurement. It is noteworthy, that in all cases, even for the freestanding graphene, the damaged area is comparable to the size of the laser irradiated spot. Finally, it should be mentioned that repeated irradiation with sub-threshold laser pulses, can generate damage over time [23, 26].

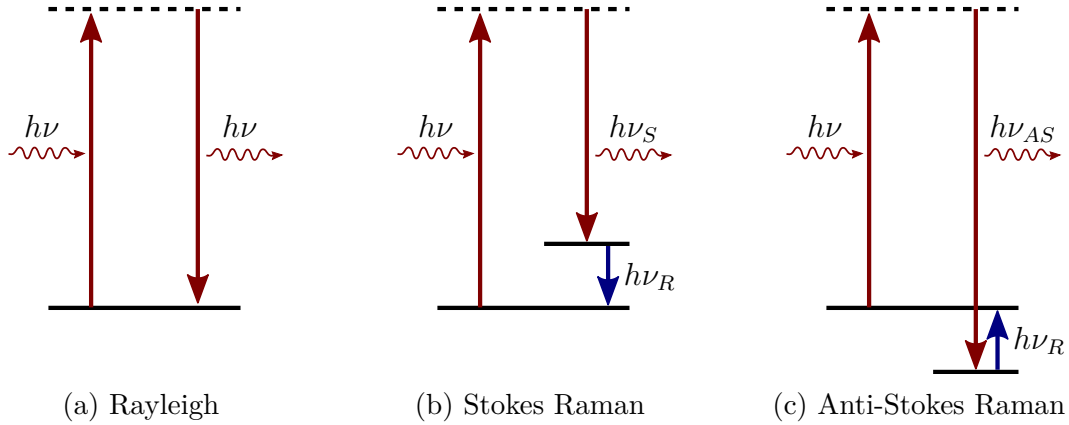


Figure 3.2: Comparison of Rayleigh and Raman scattering. The excited states are virtual states. The Raman shift is determined by the vibrational difference $h\nu_R$. Figure based on [3].

3.4 Raman Spectroscopy of Graphene

Graphene is routinely identified and analysed with the help of Raman spectroscopy. Raman spectroscopy is a popular method in material sciences and chemistry, because it allows a quick and noninvasive characterisation of samples. This is done by probing the vibrational structure of a material, which provides an excellent fingerprint for its identification.

Raman Spectroscopy is based on Raman scattering of light. The simplest, non-resonant process by which a photon can be deflected inside a material is Rayleigh scattering, shown in Figure 3.2a. In this elastic process, a photon excites an electron into a virtual state. Subsequently the electron decays back into the ground state and emits a photon with the same energy in a new direction. Opposed to this, Raman scattering is an inelastic process, where the electron does not decay back into the initial state (Figures 3.2b and 3.2c). Instead there is an energy exchange with a vibrational state of the system. In Stokes Raman scattering the electron decays into a higher energy state, resulting in the emission of a red-shifted photon. Opposed to this, anti-Stokes scattering creates a blue-shifted photon, since the electron decays into a lower energy vibration state.

To record a Raman spectrum, light with a well defined wavelength is sent into a sample and the spectral distribution of the scattered light is measured. The Raman shift, that is the energy difference between the incoming and outgoing photons, is easily calculated and usually expressed in terms of wavenumbers

$$\Delta\tilde{\nu} = \frac{1}{\lambda_{in}} - \frac{1}{\lambda_{out}}. \quad (3.6)$$

Because the Raman spectrum reflects the characteristic vibrational spectrum of the sample, it can be used for identification purposes.

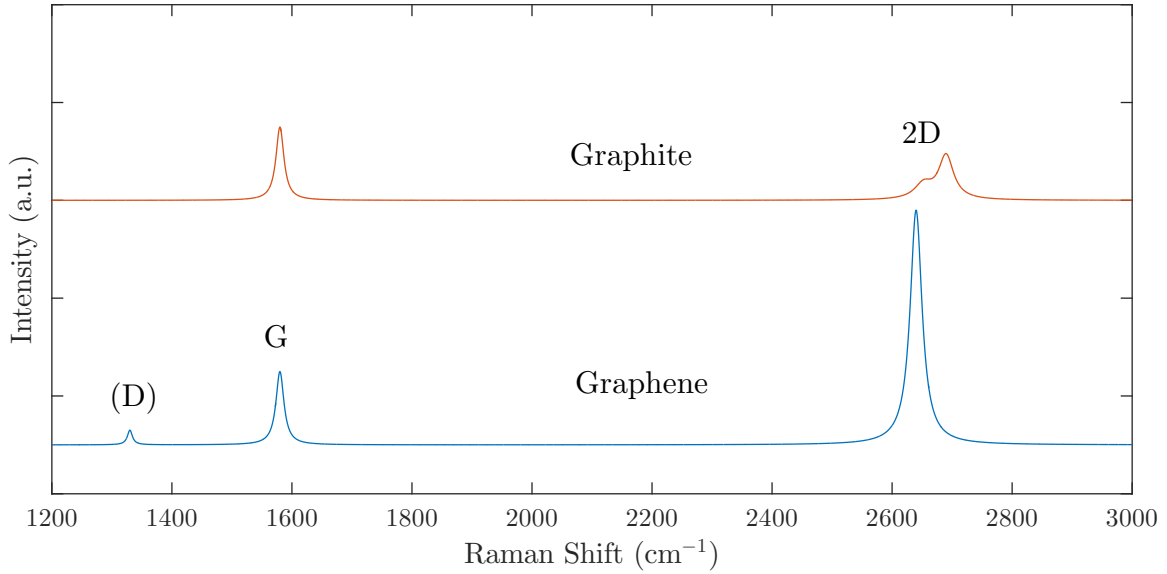


Figure 3.3: The figure shows a simplified model of the Raman spectrum of single layer graphene and graphite. Only the three most prominent features are shown. The position of the D peak is indicated, but it will only be visible in samples with defects. Experimentally acquired spectra can, for example, be found in [27, 28].

Soon after the discovery of graphene had been reported, the first measurements of graphene Raman spectra were presented [27], and Raman spectroscopy quickly became a core analysis tool. This is because the Raman spectrum of graphene has strong features, that directly indicate the number of layers, defects and purity of the graphene. These parameters are very important in order to understand and quantify experimental results. The strength of the signal and the ability to extract information linked to the electronic structure of graphene result from the fact, that Raman spectroscopy is actually resonant in graphene, because of its band structure. If it were possible to use Raman spectroscopy as an on-line analysis tool in laser plasma acceleration experiments, targets could be characterised in real time before each shot.

There are three prominent features in the graphene Raman spectrum, which are most important for a characterisation of the film quality. They are known as the D and G peaks and the $2D$ band, located at approximately 1350 cm^{-1} , 1580 cm^{-1} , and 2700 cm^{-1} , respectively (see Figure 3.3). Since the D peak and the $2D$ band are subject to dispersion, their exact location depends on the excitation wavelength. The origin of these peaks will not be discussed here, but the reader is referred to references [28] and [29] which feature detailed, theoretically supported analyses of the spectrum.

In defect-free graphene, Raman scattering linked to the D peak cannot occur. Thus the D peak will be completely suppressed in high quality graphene. Because of this link, the height of the D peak is used as a measure for the defect density in a graphene film [28]. The D peak intensity is usually compared to the intensity of the G peak. A

large ratio $I(D)/I(G)$ indicates poor quality graphene films, with a strong deviation from a continuous crystal lattice and a large signal contribution from amorphous structures. Such a signal could, for example, be generated by non uniform graphene with small single crystal domains and a large number of edge defects.

The G peak and the $2D$ band yield information about the number of graphene layers in a film. Figure 3.3 shows the Raman spectrum of graphite and single layer graphene. The latter has a strong $2D$ peak and a fairly weak G peak. When more layers are added to the graphene, the $2D$ peak starts to widen, and moves towards a higher Raman shift. At the same time the peak height decreases in comparison to the G peak, until the spectrum resembles that of graphite. In practice it appears that the layer counting accuracy is limited to differentiating single-, two-, and three to five-layer graphene. For a larger number of layers the spectrum can hardly be told apart from that of graphite [28].

4 Experimental Setup

This chapter describes the experimental setup and procedures used in this project. First, some general information about the laser system and the setup in the experimental chamber is provided. This includes a description of the graphene targets that were acquired for the measurements and a description of the target holder which was developed and manufactured to mount them in the experiment. Afterwards the strategies of the different measurements are presented.

4.1 Lund Terawatt Laser

The Lund Terawatt Laser is a high power pulsed laser system, based on chirped pulse amplification. Figure 4.1 shows the schematic layout of the amplification chain, which consists of an oscillator and four individual amplification stages. Using Ti:sapphire crystals as the gain medium in all stages, it operates at a central wavelength of 800 nm with a bandwidth of approximately 35 nm. Except for the oscillator, all amplification stages are pumped by frequency-doubled Nd:YAG lasers (532 nm). At full amplification, the pulses can reach an energy of ~ 1.5 J over 35 fs, which corresponds to a peak power of roughly 40 TW.

The oscillator forms the first component of the laser system and generates the pulses that are fed into the amplification chain. It is built as a Kerr-lens mode locked cavity, and the Ti:sapphire crystal is pumped by a continuous frequency doubled Nd:YAG laser. Pulses are generated in the oscillator at a repetition rate of 80 MHz and carry an energy of about 5 nJ. The pulse duration can be as short as 20 fs. A pulse picker is used to reduce the repetition rate to 10 Hz before the pulses are sent to the preamplifier. In the preamplifier, the pulse energy is increased to about 1 μ J.

The pulses are then guided into a grating stretcher, where the pulse duration is increased to about 450 ps. This reduces the power by more than four orders of magnitude, which is necessary to protect the optical equipment, and to suppress nonlinear interactions between the laser pulse and the gain medium in the amplifiers. Diffraction into higher orders reduces the pulse energy by approximately 50%. The next stage is a regenerative amplifier. Using a Pockels cell each laser pulse can be locked into a cavity for a certain number of roundtrips. During typically twenty passes through the intra-cavity gain medium, the pulse energy is increased to 5 mJ. The regenerative amplifier has by far the largest total gain of all stages. In the closed cavity pre-pulses get amplified very effectively. Therefore, two Pockels cells are used to temporally trim the pulses before they

4 Experimental Setup

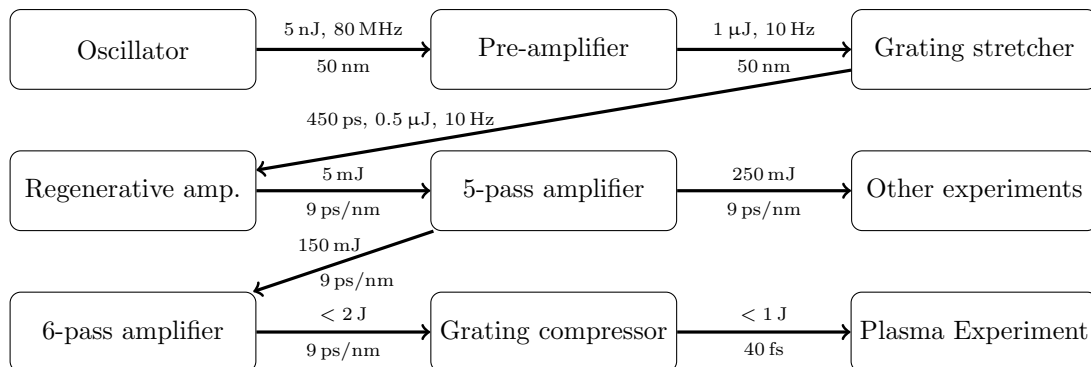


Figure 4.1: Schematic overview of the Lund Terawatt Laser.

enter the next amplifier. However, the regenerative amplifier remains the main source of ASE in the setup.

The beam is expanded to reduce the fluence, before it is guided into a five-pass amplifier, where the pulse energy is increased to 400 mJ. Each pulse is then split, and one half is sent to other experiments. The other half is spatially filtered, by focusing it through a small aperture, and then fed into the final multi-pass amplifier. Depending on the energy of the pump lasers, the pulses can reach up to more than 2 J, before the beam gets expanded to a diameter of 60 mm and sent into the compressor.

The compressor and all following systems have to be under vacuum ($\sim 10^{-4}$ mbar), because the compressed pulses are intense enough to undergo nonlinear interactions in air. After compression in the grating compressor, the pulses are typically 40 fs long and carry roughly 60% of the pre-compression energy. The compressed pulses can either be sent towards the experiment, or onto a small diagnostics table, which is not under vacuum since it is only used with attenuated laser pulses. A second order autocorrelator can be used to measure the pulse duration, and a third order autocorrelator (Sequoia, Amplitude Technologies) is available for determining the pulse contrast.

4.2 Experimental Chamber

All experiments are carried out inside a large, cylindrical vacuum chamber. The setup is optimised for investigations of laser plasma acceleration using solid targets. Some of the equipment in the chamber, like the split mirror, the ion spectrometer, and the spatial proton beam detector, have not been used in this project, but additional information on the whole setup can be found in [30]. The relevant components of the setup are explained below.

Figure 4.2 shows the inside of the experimental chamber. The laser beam enters the chamber from the side and is guided onto an off-axis parabolic mirror with a focal length $f = 15.2$ cm, which focuses the beam onto the target. The parabola can focus the beam to a FWHM spot size of approximately $3 \mu\text{m}$. The target mount is located in the centre

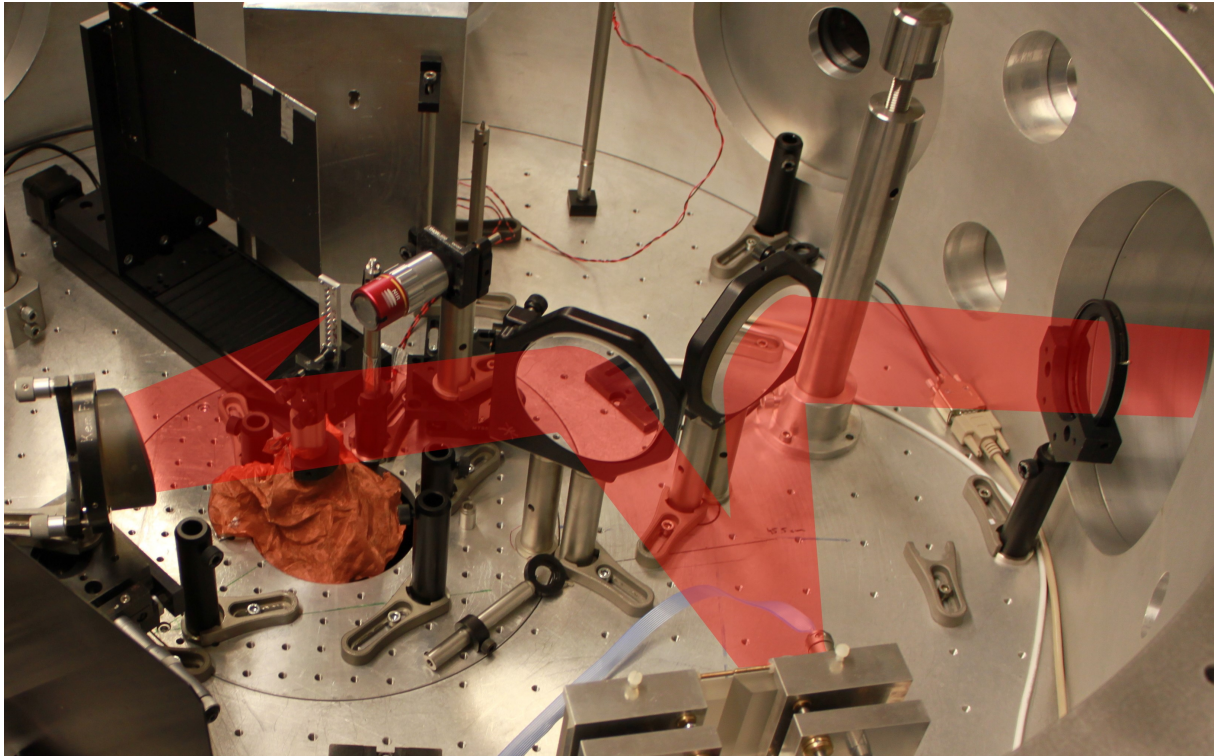


Figure 4.2: The picture shows the inside of the experimental chamber and the indicated path of the laser beam. The laser is focused onto the target with an off-axis parabolic mirror. Located behind the target is the microscope objective which is used in connection with a camera outside the chamber for laser and target alignment.

of the chamber and can be moved along three axes during vacuum conditions to select and align a certain target. Usually, the laser beam is obliquely incident on the target, but for this project the incidence was close to target normal, leaving just a small angle ($\sim 5^\circ$) to prevent a retro-reflection of the laser. This orientation makes it easier to align the small graphene targets. For the alignment of the target and the laser beam, an infinity-corrected microscope objective is used to image the back of the laser focal plane. The image is captured with a camera outside the chamber. This setup facilitates both focal spot characterisation and an accurate positioning of the target in the focal plane.

The focal spot can be corrected for aberrations with the help of a deformable mirror, which is located directly downstream of the grating compressor. A mirror can be flipped up behind the microscope objective to redirect the optical path to a wavefront sensor (SID4, Phasics). A plane close to the deformable mirror is then imaged, along the path of the laser beam, onto the sensor. Based on the wavefront signal, the thirty-two actuators on the mirror are adjusted with the help of a feedback loop, until the wave front reaches the desired shaped. This optimises the focal spot profile.

It is difficult to use the infrared light of the Terawatt Laser for the alignment of optical

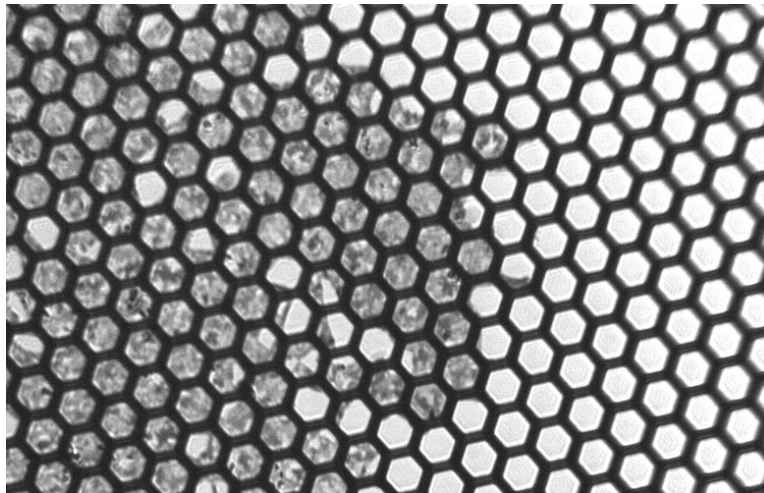


Figure 4.3: With white-light illumination through the target, it is easy to identify the graphene through the focus microscope. The contrast of the image has been digitally adjusted for clarity.

elements in the experiment. Therefore, an expanded HeNe-laser beam is used as an alignment aid. The HeNe-laser is mounted on a table next to the chamber, which also carries some cameras and the wavefront sensor. The beam is coupled into the experiment through the dichroic mirror that reflects the infrared beam into the chamber. The surface reflection of the alignment laser is used to define two reference points outside of the chamber. When the infrared beam, leaking through the mirror, is aligned onto these references, it is propagating collinear with the HeNe-laser inside the chamber. Hence, both beams will be focused onto the same point on the target. Once the infrared beam has been aligned, it can be observed with the help of the focus microscope.

Because of the very low reflectivity of graphene, the observation of freestanding graphene in the experiment should be performed in transmission. For this purpose a white-light lamp has been added to the alignment table, and can be used to send uncollimated light into the chamber, along the laser axis. The parabola focuses this light to a diffuse spot on the target, which acts as a simple back light source for the focus microscope. This has turned out to be very helpful for the alignment and identification of the graphene targets; an example can be seen in Figure 4.3. The setup can also be used to measure the transmittance of the graphene.

At the vacuum pressure found in the experiment (10^{-4} mbar), most surfaces are usually covered with a thin layer of water- and hydrocarbon molecules. If this kind of pollution also adsorbs onto graphene films is currently unclear, but due to the handling of the targets in air, surface pollution is at least possible. Protons have the highest charge to mass ratio of all ions, and are, in most acceleration mechanisms, the dominant species among the accelerated ions, unless the surface is explicitly cleaned of hydrogen before the shot.

4.2.1 Graphene Targets

Freestanding graphene is commercially available in the form of sample holders for Transmission Electron Microscopy, so called TEM grids. These TEM grids consist of a very fine metallic mesh that is covered with a single or multi-layer of graphene, providing many small cells of suspended graphene, see Figures 4.3 and 4.4. This was found to be the most practical way to acquire freestanding graphene for first tests, and two different samples were obtained during this project, one standard product and one custom design.

The standard TEM grids (Graphene on Ultra-fine 2000 Mesh Copper, TedPella) were covered with either single layer graphene or 6 to 8 layer graphene, see Figures 4.5a and 4.5b. They are based on a 6 to 8 μm thin copper mesh. For increased stability the mesh is supported by a 100 μm thick slot made from a beryllium-copper alloy. The mesh has circular apertures with a diameter of 6.5 μm . The multi-layer graphene films covers a large fraction of the TEM grids, and under the microscope the graphene appears very uniform. The single layer graphene is naturally less stable and has a lower yield rate of intact graphene cells. According to the manufacturer, the graphene is CVD-grown on copper to produce a high quality film, and subsequently transferred to the meshes in an undisclosed process.

The standard graphene TEM grids were acquired in order to learn about the handling of such targets and to assess their mechanical stability. They helped in exploring the observation methods and designing a suitable target holder, which is presented in the following section. The major problem with these grids, however, is the hole size. They are only marginally larger than the optimal laser focus diameter, and in connection with the mesh thickness, it is impossible to guide the laser through an aperture without depositing a considerable amount of pulse energy in the copper.

The custom graphene targets are based on a copper mesh with larger apertures, measuring 19 μm (Ultra Fine Hexagonal 1000 Mesh, TedPella), and were coated with nickle-grown graphene (Graphene Laboratories). The transfer process was not fully disclosed, but information from the manufacturer suggests, that it is based on the direct transfer method described in Section 3.2. Nickle-grown graphene is less uniform than copper-grown graphene and has a thickness varying randomly between one to about seven layers. In Figure 4.5c the different domains are clearly visible. Only the custom targets were used for high intensity experiments.

4.2.2 Target Holder

A specialised target holder was developed for the experiments on TEM grid-supported samples, see Figure 4.6. The holder has a base plate, into which the TEM grids are inserted. Then they are fixed in place by the lid. This geometry can be seen in Figures 4.4, 4.6 and 4.7. Up to ten targets can be mounted in the holder at the same time, in order to allow shots on a number of different targets without breaking the vacuum. Ideally a shot onto the target only causes local damage, which would allow for several shots onto

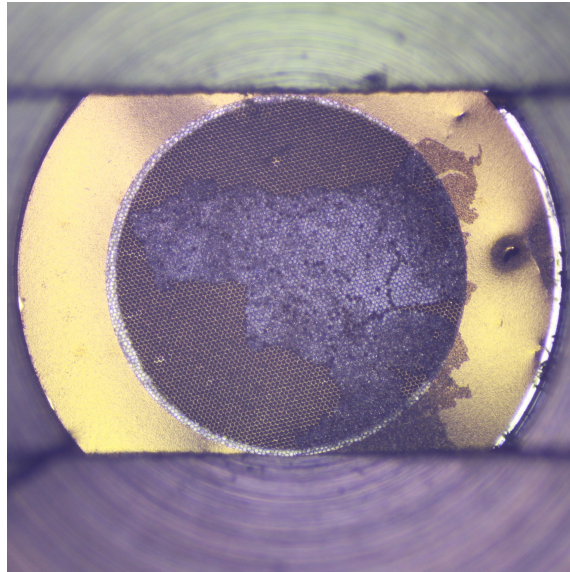
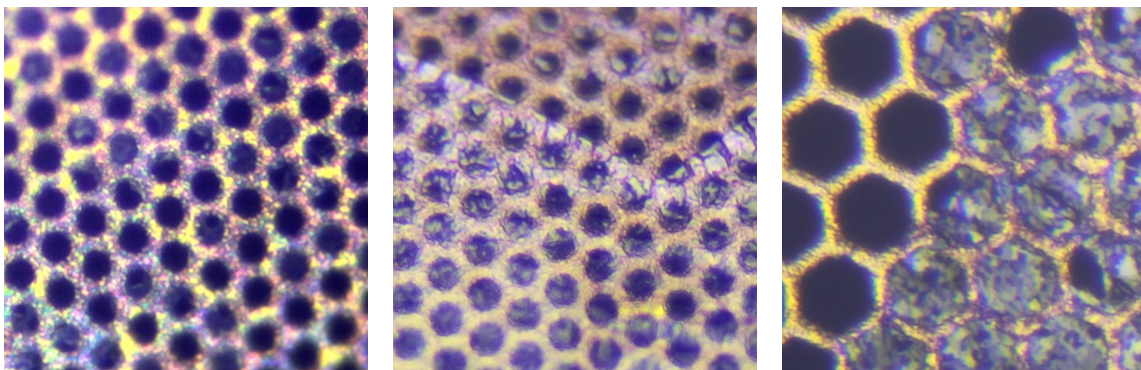


Figure 4.4: A graphene covered TEM grid (custom order), clamped in the target holder. The mesh is completely freestanding, while the rim is used to hold it in place. A graphene film can be seen, partly covering the mesh. The diameter of the mesh structure is 2 mm, the outer rim has a width of 0.5 mm.



(a) Single layer: individual holes covered by a barely visible graphene layer.

(b) 6 to 8 layer: large area uniformly covered with graphene.

(c) Custom order: graphene clearly structured in small domains.

Figure 4.5: Microscope images ($100 \times 100 \mu\text{m}^2$) of the different targets.

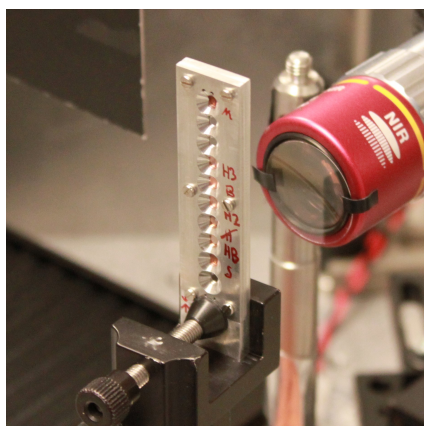


Figure 4.6: The target holder mounted in the experimental chamber.

the same TEM grid. Hence, the holder was designed in such a way that the mesh is fully accessible, and only the rim of the grid is used to fix it. TEM grids are round and standardised to a diameter of 3 to 3.05 mm. With a diameter of 3.2 mm the target slots provide a close but comfortable fit for the grids, which makes the target mounting easy, while maintaining an accurate alignment of the grid relative to the aperture in the holder. In order to allow experiments with different laser incidence angles, the apertures have a total opening angle of 90° . This also ensures that divergent particle beams will not be clipped by the target holder material.

4.3 Raman Spectroscopy for Diagnostic Purposes

The motivation for this particular experiment was to explore the feasibility of using Raman spectroscopy as an on-line diagnostic tool. HeNe-lasers are commonly used as a pump light source for Raman spectroscopy of Graphene. Since the alignment laser illuminates the target at the same point that will be hit by the high intensity pulse, one could imagine the option to record a Raman spectrum prior to the laser shot. This would provide information about the thickness of each individual targeted graphene sheet.

For this purpose the TEM grid is aligned in such a way that the HeNe-laser illuminates the cell of interest. Due to the transparency of the graphene it is easy to tell if the target is properly aligned. The laser can be seen shining through the graphene on the microscope camera; a similar situation is shown in Figure 4.8. The microscope collects the scattered light and relays it outside the chamber. A mirror can be flipped up, in order to send the collected light through a filter and into a spectrometer.

The challenge in Raman spectroscopy is to separate the very weak Raman signal from the more intense pump light and Rayleigh scattering signal. Filters are used to stop these signals at the pump wavelength from saturating the spectrometer, because that would render the detection of the Raman signal impossible. When using a 633 nm pump,

the strong features of the Graphene Raman spectrum should appear at a wavelength of approximately 703 nm and 763 nm. Most measurements were performed using a RG695 long-pass filter (3 mm, Schott). It has a transmission of 70 to 80 % for the Raman signal, while attenuating the laser wavelength by a factor of 10^{-5} . When the spectrometer was saturated, an UG7 filter (3 mm, Schott) or a RG715 filter (4 mm, Schott) were added to increase the attenuation of the primary laser signal even further. The HeNe-laser was optionally sent through an interference filter to suppress any light emission different from the desired laser line.

4.4 Measuring the Laser Pulse Induced Damage Threshold

In order to determine the laser induced damage threshold of the graphene targets, and to compare it to the measurements presented in Section 3.3, attenuated laser pulses were fired at the custom order graphene targets. The last multi-pass amplifier of the laser was turned off, and the resulting laser pulses, on target, had a maximum energy of 34 mJ. The pulse duration was 38 fs, and the focal spot size 3.3 μm FWHM. Various neutral filters were inserted into the beam path to attenuate the pulses by 4 to 7 orders of magnitude, and thus generate different on-target intensities.

To align the target to the high intensity laser, the pulse energy is reduced to a few pJ. Under these conditions it is safe to directly observe the laser beam with the focus microscope. Unattenuated pulses would burn the microscope objective and the camera. The energy is also low enough to illuminate the graphene without risking laser induced damage. Then the TEM grid can be aligned such that the laser beam hits the centre of a graphene cell, see Figure 4.8. This shot-to-shot alignment was necessary because the laser has a small drift, which could cause it to drift away from the very small target area. For some shots the target was intentionally moved out of the focal plane to change the focal spot size and thereby the fluence.

Once aligned, a reference image of the graphene was saved. The pulse energy was attenuated to the desired level, and a single pulse was fired at the graphene. Afterwards the damage can be assessed with the focus microscope and a second image was saved for comparison with the reference image. This process was repeated several times for a number of different laser intensities.

4.5 High Energy Shots on Graphene Targets

In order to look for traces of ion or proton acceleration, full energy laser pulses were directed onto the targets. This experiment aimed to clarify if there would be any acceleration with the graphene targets in the current experimental setup; it was not an implementation of CSWA.

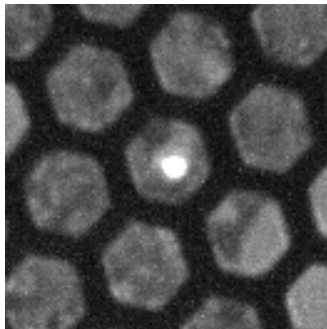


Figure 4.8: The attenuated high power laser is transmitted through the graphene, which facilitates the alignment (image size $75 \times 75 \mu\text{m}^2$).

The experiment also served the purpose of assessing the resulting damage to the TEM grids. At full power, the wings of the focal spot are intense enough to inflict laser induced damage to the mesh surrounding the targeted graphene. Shots were not only fired on graphene-covered meshes, but also on blank meshes with the same geometry, in order to compare the results. This was done, because any acceleration trace from the graphene is likely to be superimposed by traces that originate from the copper mesh.

For these measurements the pulse energy before compression was 1.3 J, the pulse duration 39 fs, and the focal spot measured approximately $4 \mu\text{m}$ (FWHM). Measured 150 ps before the peak, the pulse contrast was 4×10^{-9} . Assuming a beam transport efficiency of 45 %, this corresponds to a peak intensity of $7.8 \times 10^{19} \text{ W/cm}^2$ and an ASE intensity of $3.1 \times 10^{11} \text{ W/cm}^2$ on the target.

Instead of using the conventional scintillating detectors in the chamber, solid-state nuclear track detectors were used. These detectors are small plastic plates made of a polymer called CR-39 [31]. When nuclear radiation hits the CR-39, the radiation breaks up the polymer chains along its path. After the exposure, the plastic detectors are etched in warm sodium hydroxide (50 g NaOH, 200 g H₂O, 90 °C, 40 min). CR-39 is normally fairly inert to this etchant, but at the points where radiation broke the polymer chains, the sodium hydroxide will start to dissolve the plastic, which creates a small pit on the surface. The advantage of CR-39 is the extreme sensitivity of this detector, which can in principle record single events. Further CR-39 is relatively insensitive to electrons and x-rays, which are also produced in the laser plasma interaction, such that it primarily records the ion tracks. Heavier ions inflict a more severe damage on the polymer structure than protons and result in larger pit sizes. This allows a qualitative distinction of different ion-species on the CR-39.

For this experiment the CR-39 detectors, with a size of $50 \times 50 \times 1 \text{ mm}$, were located approximately 5 cm behind the target. One half of the plate was covered with $15 \mu\text{m}$ aluminium foil. This protects the plastic from transmitted laser light, and also stops protons with a kinetic energy $\lesssim 1 \text{ MeV}$ [32]. By leaving half of the detector uncovered, it is assured that potentially generated low energy protons are still detected.

5 Results & Conclusion

This chapter summarises the experimental results of the project. The first section contains some general remarks about the targets and their use in the experimental chamber. After that the different measurements are discussed. The final section contains a conclusion of the project.

5.1 Graphene Targets

The experimental work conducted during this project has successfully demonstrated the general feasibility of handling freestanding graphene targets in the existing experimental setup. With the help of the specially designed target holder, it is now easy to mount TEM grid supported graphene targets in the experiment. Since TEM grids are available with a wide range of different mesh geometries and sizes, this creates a flexible base for the development of future targets. As shown in Figure 4.3, the chamber microscope can be used to observe and align the targets on the large mesh. For the smaller grid the identification is more difficult, because less light is passing through the apertures, which degrades the contrast. One initial concern was, if the graphene would be able to withstand the strong airflow and vibrations during the evacuation and ventilation of the vacuum chamber, but samples of all three different target grids have been subject to several vacuum cycles and show no signs of pumping-related damage.

The transmittance of the nickle grown graphene on the larger mesh was measured, in order to estimate the number of layers. Under a normal microscope the graphene appears very flaky, see Figure 4.5c, which indicates that it is composed of domains with different numbers of layers. A transmittance measurement should validate this impression and allow to estimate the number of layers according to Equation 3.5.

The result of such a transmittance measurement is shown in Figure 5.1. Some of the cells were not covered by graphene and show a transmission close to 100 %, which indicates that the mesh structure does not interfere with the measurement. According to the manufacturer, the graphene should have a maximum of seven layers. Estimating an extreme scenario of ten layers, accounting for the increased absorption of blue light ($\sim 3\%/layer$), and adding another 10 % absolute error margin, the transmission should never fall below 60 %. Yet, many cells on the mesh show even lower transmission. A number of factors may have contributed to this result. Possibly the surface of the graphene is contaminated. Such contamination could either be formed by material residues from the manufacturing process, or the handling in normal atmosphere results in the adsorption of water and hy-

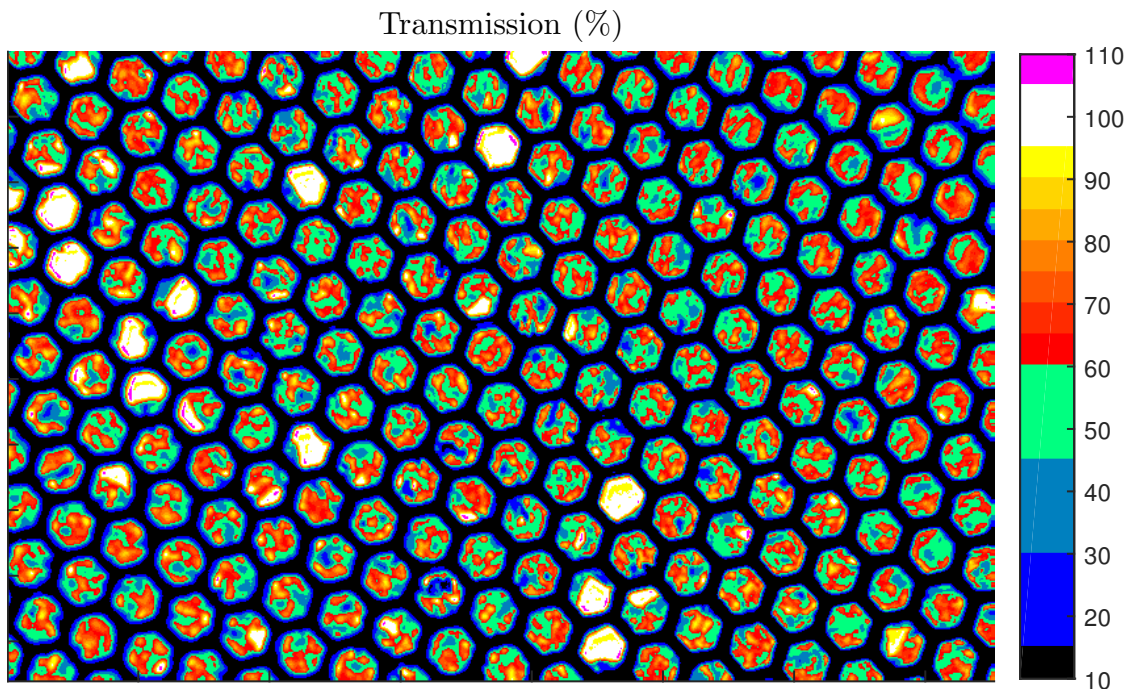


Figure 5.1: The plot shows a transmission map of a graphene covered TEM grid. Some mesh cells were uncovered and show approximately 100% transmission. The graphene-covered cells appear strongly structured and have a wide range of transmittance values.

drocarbon molecules on the graphene. Another possibility is that the graphene film has folds and wrinkles. This would create spots with larger numbers of layers and an increased film thickness. In order to ensure unambiguous and stable experimental conditions in the future, a dedicated material analysis of the graphene target seems recommendable. Alternatively and on-line monitoring of the graphene at the designated target position could determine the current target characteristics.

5.2 Raman Spectroscopy

The attempt to record a Raman spectrum with the alignment laser and the focus microscope was not successful using the equipment at hand during the experiment. Different filter combinations and alignments of the spectroscope were tested but none provided a distinguishable Raman signal. The reason for this is most likely the very limited collection efficiency of the focus microscope setup. Conventional Raman microscopes often use 100x microscope objectives, with a very short working distance, both to focus the laser onto the sample and to collect the back-scattered light. Compared to this, the open setup in the present study collects only a small fraction of the scattered light, due to the large

distance between graphene and objective. Further, this setup was not sufficiently shielded from stray light, such that there will always be a small amount of background light that is focused into the spectrometer. A possible improvement to the current situation would be to increase the collection efficiency of the microscope, by choosing another objective. In addition to that, a more sensitive detector could be used in combination with notch filters that isolate the Raman peaks from all kinds of background light.

5.3 Laser Induced Damage Threshold

The threshold measurement for laser induced damage of graphene was evaluated by comparing the size of the damaged area to the peak intensity of the laser pulse. To measure the damage size, images of the graphene before and after the laser shot were compared as shown in Figure 5.2. The laser intensity and fluence were estimated with the equations presented in Section 2.1.1, assuming a pulse energy of $E_p = 34 \text{ mJ} \cdot 10^{-\text{OD}}$, where OD is the optical density of the filter. The results are presented in Figure 5.3.

The experimental data indicates, that the damage threshold fluence of the graphene targets is located approximately between 70 to 130 mJ/cm², or 1.7×10^{12} to 3.2×10^{12} W/cm² in terms of intensity. A more precise estimate would require a higher density of measurement points close to the threshold. These fluence values for a multi-layer graphene target are slightly lower than previously reported laser induced damage thresholds for single layer graphene on a substrate, which were presented in Section 3.3. There is a particularly good agreement with the threshold for freestanding graphene of 86 mJ/cm² reported in [24].¹

In Section 3.3 it was discussed, that for pulse durations up to the nanosecond scale, the damage threshold appears to depend primarily on the fluence, and not the intensity. This measurement indicates that the focused ASE, with a fluence of several J/cm² (cf. Section 2.1.2), will initiate the ablation of the graphene before the main pulse arrives. An interesting follow up experiment would be to bypass the pulse compressor and validate the threshold value for stretched pulses, with several hundreds picoseconds pulse length. That would be a more accurate representation of the ASE.

At higher pulse energies the size of the damaged area increases. This is attributed to the fact, that the area of the laser spot which is intense enough for ablation, scales with the pulse energy. Further support for this assumption is shown in Figure 5.4, which shows that the damage for the highest energy shot investigated has a similar shape as the saturated image of the laser pulse. This suggests, that the fluence in the outer regions of the spot profile was high enough to ablate the graphene at this filter setting. It is interesting to note that the graphene is otherwise extremely stable and the damage is strictly confined to the high fluence areas. It was expected that the laser ablation would blow out the graphene at least within one mesh cell. Yet, at sufficiently low energies, this

¹The threshold value in [24] was given in terms of the average fluence and converted to the peak fluence definition in this report.

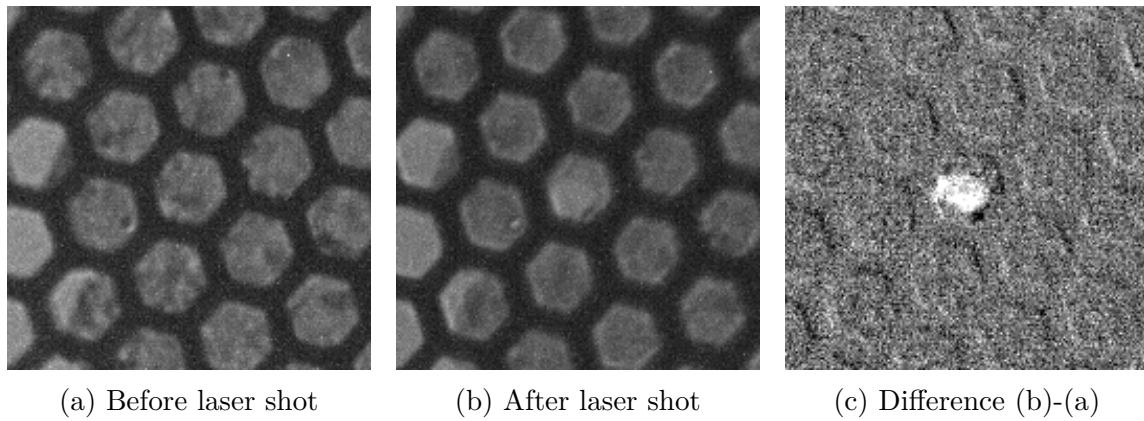


Figure 5.2: The images ($100 \times 100 \mu\text{m}^2$) visualise how the laser induced damage of the graphene was measured. In the difference image, the damage size can be determined clearly.

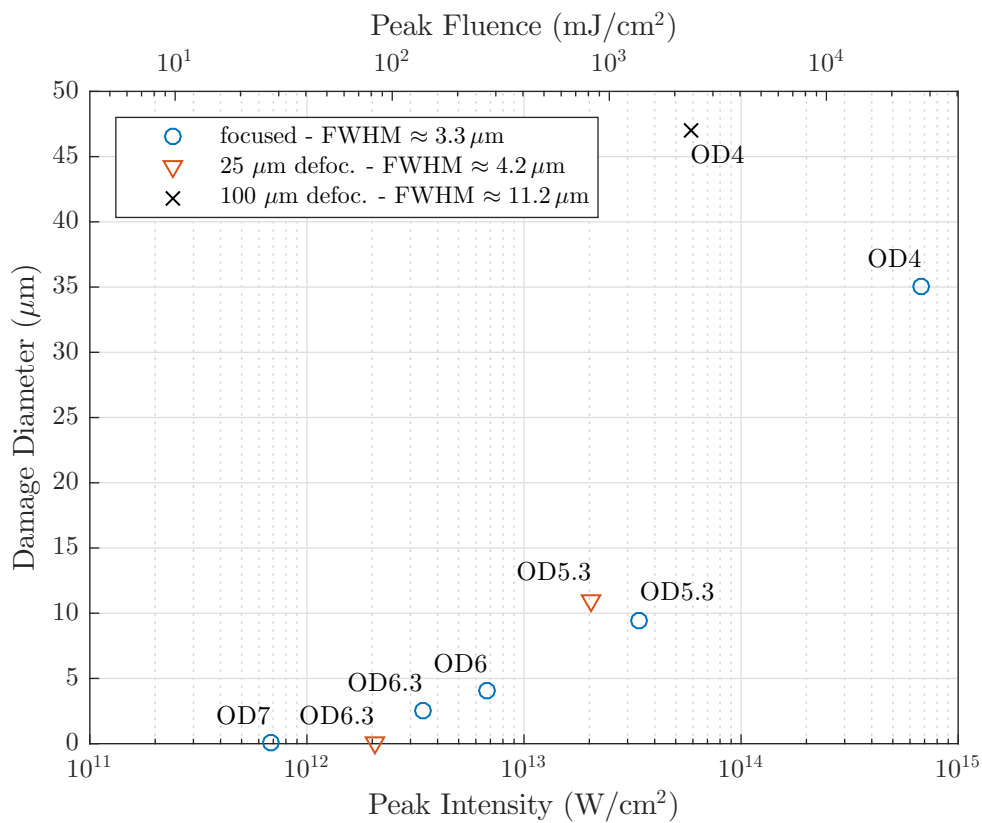
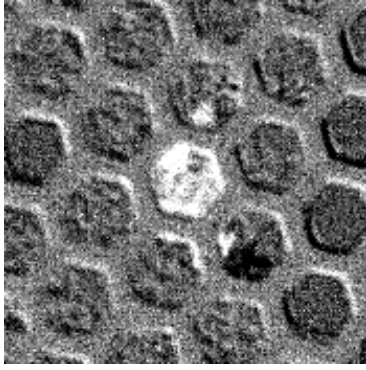
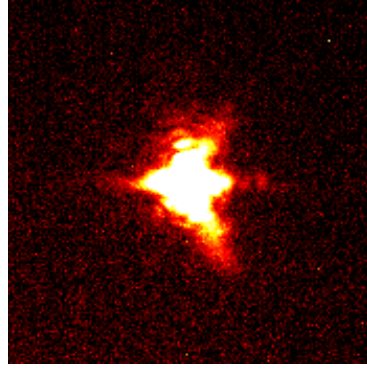


Figure 5.3: The plot shows the size of the damaged area depending on the peak fluence and intensity of the laser pulse. The labels next to the data points show the total optical density of the filters that were used to attenuate the pulses.



(a) Damage created with a pulse energy of $3.4 \mu\text{J}$.



(b) A saturated image of the focus reveals the non-Gaussian profile of the wings of the focal spot.

Figure 5.4: The images ($100 \times 100 \mu\text{m}^2$) demonstrate the correspondence between the profile of the laser focus and the shape of the graphene damage.

study shows that freestanding graphene can basically be micro machined with the laser, without damaging the surrounding material.

5.4 High Energy Shots

At ultra high intensities, the extended wings of the focal spot are intense enough to damage not only the graphene, but also the surrounding copper mesh. Figure 5.5 shows the damage inflicted to the TEM grid with a full power shot. With just about $250 \mu\text{m}$, the holes in the TEM grids are far smaller than the holes left behind in conventional target foils ($\gtrsim 1 \text{mm}$) at the same energy, because only the edge of the focal spot overlaps with the mesh. Further, the graphene film was only removed in vicinity to the hole in the mesh, possibly due to a shock wave that may have propagated through the grid. Farther away from the impact hole ($\sim 500 \mu\text{m}$), the graphene appeared to be intact. In principle a single TEM grid can thus be used for several shots.

However, the structural damage suggests that the mesh close to the target cell has been turned into copper plasma. This plasma can mix with the graphene plasma and interfere with the laser graphene interaction. Therefore it may be necessary to suspend the graphene over even larger areas. The situation could also be improved by using a stronger focusing mirror, to reduce the focal spot size. Additionally, it has to be considered that the ASE may ionise the graphene early and the plasma will then have time to expand.

Despite these limitations, the shots onto the TEM grids have produced some interesting results. Figure 5.6a shows a photo micrograph of an etched CR-39 detector. The image illustrates the effect of the aluminium foil filter. The part of the CR-39 that was directly exposed to incoming particles is strongly etched. There are so many pits in this area that

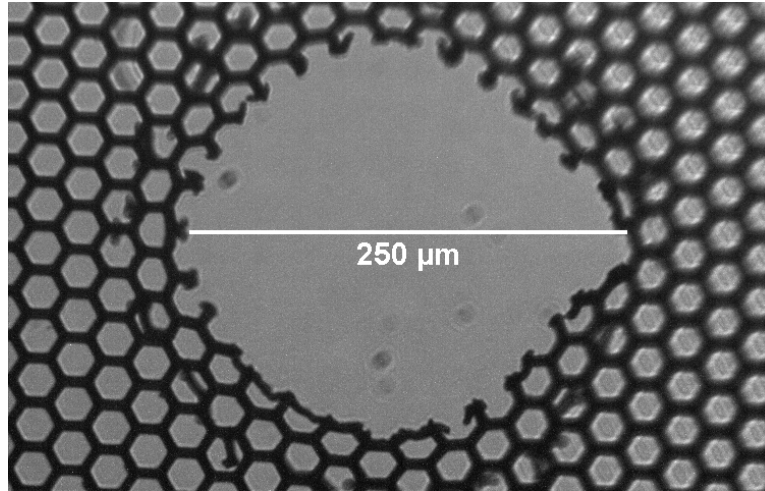
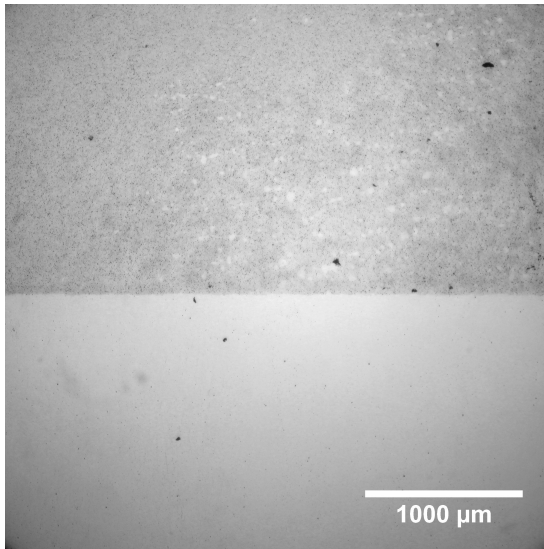


Figure 5.5: The image shows the characteristic damage to the TEM grid after a high intensity shot.

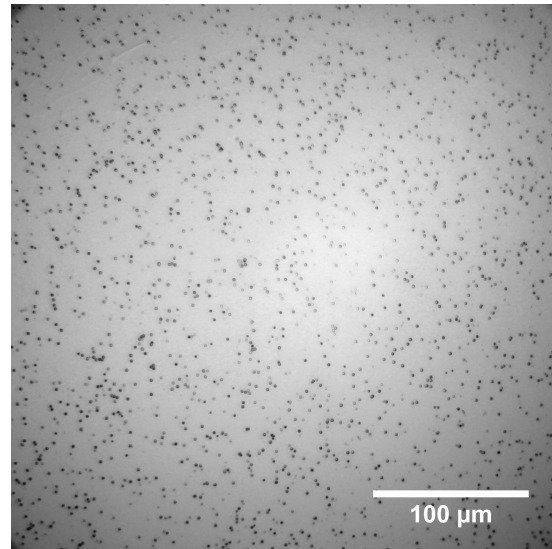
they overlap and create a diffuse background. In the aluminium-shielded part, this effect is not observed. In this particular shot a laser pulse was guided through a blank TEM grid to obtain a reference of the signal generated by the interaction with the copper mesh. The blurry background was observed with varying intensity on all CR-39 detectors, regardless of the target. Most likely this is the result of low energy protons. It was considered that the transmitted part of the laser pulse may have burned the CR39, but this signal is spread fairly uniformly over the entire uncovered part of the detector and therefore bigger than the laser beam. Furthermore, the same background signal was found to be even stronger in another shot, where the laser had struck the copper mesh directly and should not have been transmitted at all.

The direct shot onto the copper mesh was unintended and occurred because of temporary target motion. Nevertheless, it created some interesting signatures on the CR-39. It is assumed, that the interaction with the copper foil has resulted in TNSA, target normal sheath acceleration, the most common acceleration mechanism for solid targets. It creates mostly protons with an energy of a few MeV. The traces of these protons can be seen in Figure 5.6b, which shows a part of the detector that was covered with aluminium foil. Because the low energy proton background has been filtered out, it is possible to identify individual proton hits in the CR-39, corresponding to protons with energies $\gtrsim 1$ MeV.

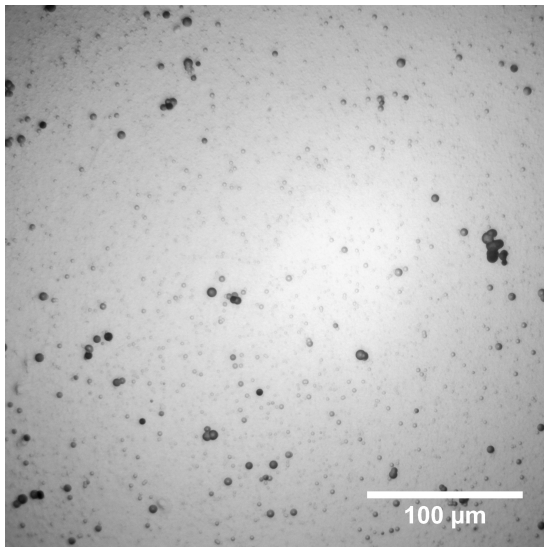
Figure 5.6c illustrates the ability of CR-39 to differentiate between ion species. The pits in the surface have distinctly different sizes, and appear to fall into different classes. While no quantitative analysis has been performed, the most likely ion species in this experiment are obviously carbon, copper, and protons and oxygen (from adsorbed water molecules). This means that even at these non-optimal conditions some ions were accelerated, in addition to the expected protons. It is unknown if they come from the graphene or the copper mesh.



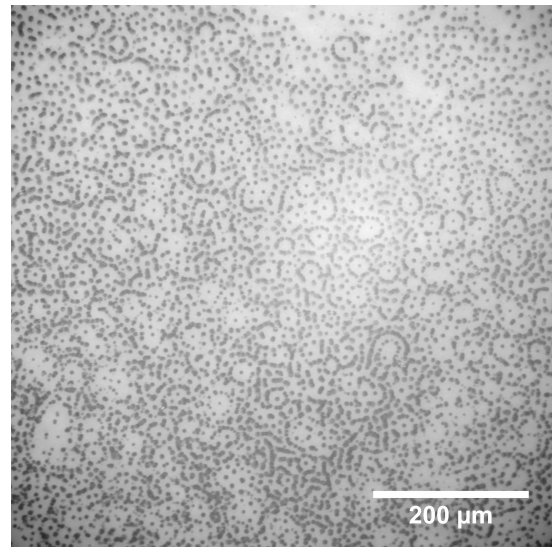
(a) Large scale signal distribution on the CR-39 detector, after a shot through a blank TEM grid. The lower half was covered by aluminium foil. The pit density in the upper half is very high, such that it looks continuous in this image.



(b) Proton signal on the aluminium-covered part of a CR-39 detector. This was the result of shooting directly onto the copper structure of a TEM grid.



(c) Traces of different ion species on the uncovered part of a CR-39 detector, after a shot on a graphene-covered mesh cell.



(d) Signal found on the rear side of a CR-39 detector after a shot on graphene. A clear structure can be seen in the distribution of the pits.

Figure 5.6: The images show different characteristics of the signals found on the CR-39 detectors.

Interesting features were also found on the rear side of the CR-39 detectors. There is an accumulation of pits close to the beam axis on all detectors, but only in the unshielded part. Some of them show interesting structures. An example is given in Figure 5.6d. So far there is no definitive explanation for these signals, and the intriguing structure of the pattern motivates further investigations. A possible lead is the following observation: The CR-39 detectors were mounted on a black-painted metal shield. After the shots, there were burn marks in the paint layer, and black stains on the CR-39. The stains were easy to remove with ethanol, but the burn marks suggest that a significant fraction of the laser pulse was transmitted through the target and the CR-39. It remains unclear if this is linked to the pits on the rear side, and would also not explain the distinct pattern.

While the presented results are interesting, they definitely need to be validated and extended under optimised experimental conditions. At the moment the ASE may blow up the graphene before the arrival of the main pulse, and a significant fraction of the accelerated particles probably arises from the copper mesh. A dedicated and precise study of graphene requires an adjustment of the experimental setup and the target geometry.

5.5 Conclusion

In this project, freestanding graphene has successfully been implemented as a novel target material for future experiments on laser plasma acceleration. By choosing TEM grids as a support structure for suspended graphene and developing a suitable target mount, a simple and flexible target system has been created, which can be used with the existing experimental setup. The graphene is stably mounted in the experiment, and the TEM grid system offers the opportunity to simply create new targets on different mesh geometries. Further it has been demonstrated that the graphene targets can be observed and aligned with a small modification of the focus microscope.

The conducted experiments provide important information on necessary improvements and follow-up investigations. It is suggested by the transmission measurement that the graphene target needs to be monitored on-line or substituted with a higher quality product, in order to create controlled and reliable experimental conditions. Raman spectroscopy can be a practical diagnostic tool, but requires dedicated modifications of the experimental setup. If the transmission measurement can be independently confirmed to provide an accurate layer counting, it may replace the use of Raman spectroscopy as an easier and more accurate diagnostic tool for this purpose. In the long run, Raman spectroscopy still seems to be a valuable tool, because of its ability to characterise not only the thickness but also the quality of graphene targets. The laser induced damage threshold was measured successfully. It underlines the importance of reducing the ASE, in order to prevent graphene ablation before the arrival of the main pulse. The high intensity experiments have demonstrated that the utilised mesh is too fine, and the mesh size needs to be increased to prevent an ionisation of copper. Nevertheless, the detectors showed some interesting signatures that motivate a validation under optimised conditions.

6 Outlook

This project has demonstrated the general feasibility of working with graphene targets in connection to ultra-high intensity laser experiments. The practical experience collected during the work with the targets, paired with the information gathered in this report, form a helpful foundation for the design of upcoming experiments. With some adjustments to the current target design, high-quality freestanding graphene should be available for dedicated studies of the laser plasma interactions in the foreseeable future. In this context, it could be very instructive to attempt an in-house fabrication of the targets. Graphene and blank TEM grids are commercially available and could be used for studies on target production with different mesh geometries.

Two devices, that are currently being developed within the ultra-high intensity group, will significantly support the studies on graphene. It is planned to include a double plasma mirror into the laser setup (cf. Section 2.1.2). The double plasma mirror may decrease the ASE level by roughly three orders of magnitude, which means that the ionisation of the graphene would occur much closer to the arrival of the pulse peak, which gives the plasma less time to expand. The second development concerns a new detector. A Thomson parabola uses parallel magnetic and electric fields to create an ion species-sensitive spectrometer. Such a device would be very useful to measure the contribution of different species to the accelerated particles. This will help to understand how graphene, surface-adsorbed water, and the supporting mesh interact during the acceleration process.

With an improved experimental setup there are a number of interesting measurements to be conducted. Obviously, the general properties of the particle beams, generated from a graphene target, should be characterised and compared to those of other ultra-thin materials. Aiming at a better understating of the acceleration mechanism, and the experimental development towards CSWA, it is also important to look at the plasma and the interaction with the laser beam itself. Such studies could include the measurement of the onset of relativistic induced transparency, by measuring the transmission of the laser pulse through the plasma with time resolution. The plasma density can be measured with interferometric methods which yields complementary information about the expansion of the graphene plasma.

These measurements will help to assess if graphene offers significant advantages over established target materials, and if it is a suitable choice for the ultra-thin film required for a CSWA target assembly.

Acknowledgements

First of all, I would like to express my gratitude to my supervisor, Claes-Göran Wahlström, for inviting me to work on this very interesting project. Thank you for your advice and guidance throughout this project and for always creating a welcoming and encouraging working atmosphere. I also want to thank Lovisa Senje, Kristoffer Svensson, and Malay Dalui for introducing me to the experimental setup, supporting me with my measurements, and contributing with valuable input during plenty of fruitful discussions. Let me also point out my appreciation for the very instructive discussions that I had with Anders Persson, who always willingly shared his knowledge of the Lund Terawatt Laser and all the surrounding systems. Further, I would like to thank Olle Lundh, Martin Hansson, Henrik Ekerfelt, Isabel Gallardo Gonzalez, Jonas Björklund Svensson, and Philip Siederer for many interesting discussions and helpful guidance during our group meetings and in the lab. It has been a great pleasure to work with everyone in the Ultra-high Intensity Group; thanks for making me feel welcome at all times. I also want to use the chance to thank everyone in the PLIONA collaboration, for extremely informative presentations and discussions during the collaboration meeting. At this point, I also wish to thank my office mates, Samuel Bengtsson and Ivan Sytsevich, and also Neven Ibrakovič, Emma Simpson, and Jan Lahl, for many friendly and scientific conversations, cosy fika-breaks, and occasional office-shenanigans. Finally I would like to give a big shout-out to everyone in the Atomic Physics Division for creating such an amazing and supportive working environment.

References

- [1] H. Daido, M. Nishiuchi, and A. S. Pirozhkov, “Review of laser-driven ion sources and their applications”, [Reports on Progress in Physics](#) **75**, 056401 (2012).
- [2] F. Mackenroth, A. Gonoskov, and M. Marklund, “Chirped-standing-wave acceleration of ions with intense lasers”, [Physical Review Letters](#) **117**, 104801 (2016).
- [3] B. E. A. Saleh and M. C. Teich, *Fundamentals of photonics*, Wiley Series in Pure and Applied Optics (Wiley, 2013).
- [4] D. Strickland and G. Mourou, “Compression of amplified chirped optical pulses”, [Optics Communications](#) **56**, 219–221 (1985).
- [5] K. Svensson, “Experiments on laser-based particle acceleration beams of energetic electrons and protons”, PhD thesis (Lund University, 2016).
- [6] B. Dromey, S. Kar, M. Zepf, and P. Foster, “The plasma mirror—a subpicosecond optical switch for ultrahigh power lasers”, [Review of Scientific Instruments](#) **75**, 645 (2004).
- [7] P. Gibbon, *Short pulse laser interactions with matter* (Imperial College Press London, Sept. 2005).
- [8] V. Kiisk, T. Kahro, J. Kozlova, L. Matisen, and H. Alles, “Nanosecond laser treatment of graphene”, [Applied Surface Science](#) **276**, 133–137 (2013).
- [9] W. L. Kruer, *The physics of laser plasma interactions*, Frontiers in Physics (Westview Press, 2003).
- [10] S. Palaniyappan, B. M. Hegelich, H.-C. Wu, D. Jung, D. C. Gautier, L. Yin, B. J. Albright, R. P. Johnson, T. Shimada, S. Letzring, D. T. Offermann, J. Ren, C. Huang, R. Hörlein, B. Dromey, J. C. Fernandez, and R. C. Shah, “Dynamics of relativistic transparency and optical shuttering in expanding overdense plasmas”, [Nature Physics](#) **8**, 763–769 (2012).
- [11] B. M. Hegelich, B. J. Albright, J. Cobble, K. Flippo, S. Letzring, M. Paffett, H. Ruhl, J. Schreiber, R. K. Schulze, and J. C. Fernández, “Laser acceleration of quasi-monoenergetic MeV ion beams”, [Nature](#) **439**, 441–444 (2006).

- [12] B. Gonzalez-Izquierdo, M. King, R. J. Gray, R. Wilson, R. J. Dance, H. Powell, D. A. Maclellan, J. McCreadie, N. M. H. Butler, S. Hawkes, J. S. Green, C. D. Murphy, L. C. Stockhausen, D. C. Carroll, N. Booth, G. G. Scott, M. Borghesi, D. Neely, and P. McKenna, “Towards optical polarization control of laser-driven proton acceleration in foils undergoing relativistic transparency”, *Nature Communications* **7**, 12891 (2016).
- [13] K. Novoselov, A. Geim, S. Morozov, D. Jiang, Y. Zhang, S. Dubonos, I. Grigorieva, and A. Firsov, “Electric field effect in atomically thin carbon films”, *Science* **306**, 666–669 (2004).
- [14] C. J. Shearer, A. D. Slattery, A. J. Stapleton, J. G. Shapter, and C. T. Gibson, “Accurate thickness measurement of graphene”, *Nanotechnology* **27**, 125704 (2016).
- [15] A. B. Kuzmenko, E. Van Heumen, F. Carbone, and D. Van Der Marel, “Universal optical conductance of graphite”, *Physical Review Letters* **100**, 2–5 (2008).
- [16] R. R. Nair, P. Blake, a. N. Grigorenko, K. S. Novoselov, T. J. Booth, T. Stauber, N. M. R. Peres, and a. K. Geim, “Fine structure constant defines visual transparency of graphene”, *Science* **320**, 2008 (2008).
- [17] X. Li, W. Cai, J. An, S. Kim, J. Nah, D. Yang, R. Piner, A. Velamakanni, I. Jung, E. Tutuc, S. K. Banerjee, L. Colombo, and R. S. Ruoff, “Large-area synthesis of high-quality and uniform graphene films on copper foils”, *Science* **324**, 1312–1314 (2009).
- [18] A. Reina, X. Jia, J. Ho, D. Nezich, H. Son, V. Bulovic, M. S. Dresselhaus, and K. Jing, “Large area, few-layer graphene films on arbitrary substrates by chemical vapor deposition”, *Nano Letters* **9**, 30–35 (2009).
- [19] A. Reina, H. Son, L. Jiao, B. Fan, M. S. Dresselhaus, Z. Liu, and J. Kong, “Transferring and identification of single- and few-layer graphene on arbitrary substrates”, *Journal of Physical Chemistry C* **112**, 17741–17744 (2008).
- [20] Y.-M. Chen, S.-M. He, C.-H. Huang, C.-C. Huang, W.-P. Shih, C.-L. Chu, J. Kong, J. Li, and C.-Y. Su, “Ultra-large suspended graphene as a highly elastic membrane for capacitive pressure sensors”, *Nanoscale* **8**, 3555–3564 (2016).
- [21] W. Regan, N. Alem, B. Alemán, B. Geng, Ç. Girit, L. Maserati, F. Wang, M. Crommie, and A. Zettl, “A direct transfer of layer-area graphene”, *Applied Physics Letters* **96**, 113102 (2010).
- [22] B. Alemán, W. Regan, S. Aloni, V. Altoe, N. Alem, C. Girit, B. Geng, L. Maserati, M. Crommie, F. Wang, and A. Zettl, “Transfer-free batch fabrication of large- area suspended graphene membranes”, *ACS Nano* **4**, 4762–4768 (2010).
- [23] A. Roberts, D. Cormode, C. Reynolds, T. Newhouse-Illige, B. J. Leroy, and A. S. Sandhu, “Response of graphene to femtosecond high-intensity laser irradiation”, *Applied Physics Letters* **99**, 51912 (2011).

- [24] J. H. Yoo, J. Bin In, J. Bok Park, H. Jeon, and C. P. Grigoropoulos, “Graphene folds by femtosecond laser ablation”, *Applied Physics Letters* **100**, 233124 (2012).
- [25] H. O. Jeschke, M. E. Garcia, and K. H. Bennemann, “Theory for the ultrafast ablation of graphite films”, *Physical Review Letters* **87**, 015003 (2001).
- [26] V. D. Frolov, P. A. Pivovarov, E. V. Zavedeev, A. A. Khomich, A. N. Grigorenko, and V. I. Konov, “Laser-induced local profile transformation of multilayered graphene on a substrate”, *Optics and Laser Technology* **69**, 34–38 (2015).
- [27] A. C. Ferrari, J. C. Meyer, V. Scardaci, C. Casiraghi, M. Lazzeri, F. Mauri, S. Piscanec, D. Jiang, K. S. Novoselov, S. Roth, and A. K. Geim, “Raman spectrum of graphene and graphene layers”, *Physical Review Letters* **97**, 187401 (2006).
- [28] A. C. Ferrari, “Raman spectroscopy of graphene and graphite: disorder, electron-phonon coupling, doping and nonadiabatic effects”, *Solid State Communications* **143**, 47–57 (2007).
- [29] L. M. Malard, M. A. Pimenta, G. Dresselhaus, and M. S. Dresselhaus, “Raman spectroscopy in graphene”, *Physics Reports* **473**, 51–87 (2009).
- [30] B. Aurand, M. Hansson, L. Senje, K. Svensson, A. Persson, D. Neely, O. Lundh, and C.-G. Wahlström, “A setup for studies of laser-driven proton acceleration at the Lund Laser Centre”, *Laser and Particle Beams* **33**, 59–64 (2014).
- [31] D. Henshaw, N. Griffiths, and O. A. Landen, “A method of producing thin CR-39 plastic nuclear track detectors and their application in nuclear science and technology”, *Nuclear Instruments and Methods* **180**, 65–77 (1981).
- [32] M. Berger, J. Coursey, M. Zucker, and J. Chang, *ESTAR, PSTAR, and ASTAR: Computer programs for calculating stopping-power and range tables for electrons, protons, and helium ions*, (2005) <http://physics.nist.gov/Star> (visited on 12/09/2016).